

Chapter 17

Synthetic Aperture Radar*

Roger Sullivan

Institute for Defense Analyses

Most of the discussion in this Handbook concerns *real aperture radar (RAR)*, where the antenna is a physical object that first emits, and then collects, the radiation. We turn our attention to the case where the antenna moves to cover a *synthetic aperture*, thus producing *synthetic aperture radar (SAR)*. This overview is based on Sullivan¹ and Cutrona^{2†}; more detailed treatments are also provided in the literature.^{3–11}

17.1 BASIC PRINCIPLE OF SAR

For airborne or spaceborne ground-mapping radar, there has been continuous desire to achieve finer resolution. We shall use the term *range resolution* to mean the resolution along the line-of-sight (LOS) from the radar to the target region and *crossrange resolution* to mean the resolution along the direction perpendicular to the LOS and parallel to the ground. The former is also frequently termed *downrange resolution* to emphasize that it is along the LOS. Crossrange resolution is also frequently called *azimuth resolution*, since it is measured along a line obtained by holding range constant and varying the azimuth (as measured from the physical antenna) of the LOS. If (and only if) the LOS remains perpendicular to the direction of flight, range resolution is sometimes called *cross-track resolution*, and crossrange resolution is sometimes called *along-track resolution*.

With respect to SAR resolution, the preferred terms are *fine* and *coarse*. Better resolution is *finer*, not *greater*; poorer resolution is *coarser*, not *less*. In this way ambiguity in terminology can be avoided. Of course, in practice the terms *high-resolution* (fine resolution) and *low-resolution* (coarse resolution) are often used without ambiguity.

Crossrange resolution was initially achieved by use of a narrow beam. The beam-width (in radians) θ_B of an aperture antenna is given approximately by the wavelength

* The present chapter draws significantly from Dr. Sullivan's book, *Radar Foundations for Imaging and Advanced Concepts*, Raleigh, NC: SciTech Publishing, 2004. Dr. Sullivan is grateful to SciTech for permission to quote considerable material from the chapters on SAR. He is also grateful to Mr. Michael Tuley (Institute for Defense Analyses) for reviewing the manuscript prior to publication and suggesting many improvements.

† In the first two editions of this Handbook, the chapter on SAR was written by Dr. Louis J. Cutrona, who is now deceased. In 1988, Dr. Sullivan had the privilege of working with Dr. Cutrona at the Environmental Research Institute of Michigan, Ann Arbor (now General Dynamics, Ypsilanti), and is grateful for having learned much from him concerning SAR.

λ divided by the aperture diameter: $\theta_B \approx \lambda/D$. The corresponding linear crossrange resolution at range R is then

$$\delta_{cr} \approx \frac{R\lambda}{D} \quad (\text{real aperture}) \quad (17.1)$$

For example, if $\lambda = 3$ cm (X band) and $D = 2$ m, $\theta_B \approx 0.015$ radians. At a range of $R = 100$ km, the crossrange resolution would be $R \theta_B \approx 1.5$ km, hardly fine enough to resolve such targets as buildings and vehicles. However, by using appropriate coherent processing, an aperture of modest size may be moved (e.g., by an aircraft or spacecraft—referred to as the *platform*) along a path in space—a *synthetic aperture*—and may achieve crossrange resolution comparable to what would, in principle, be achieved by a real aperture with a length equal to the path length (synthetic aperture) L_{SA} :

$$\delta_{cr} \approx \frac{R\lambda}{2L_{SA}} \approx \frac{\lambda}{2\Delta\theta} \quad (\text{synthetic aperture}) \quad (17.2)$$

where $\Delta\theta$ is the synthetic aperture angle, i.e., the angle subtended by the synthetic aperture as seen from the target area. The additional factor of two in the denominator (compared with Eq. 17.1) occurs because of the SAR processing and will be discussed. For example, for a path length of 5 km, the crossrange resolution for the case discussed above would be ≈ 30 cm, clearly a superb improvement over the real-aperture case.

17.2 EARLY HISTORY OF SAR

The original concept of SAR was first described by Carl Wiley of Goodyear in 1951.¹² He called it *doppler beam sharpening (DBS)*. Later, the doppler beam sharpening mode of SAR was introduced as the name for a variable squint angle mode that produced a partial plan-position indicator (PPI) display. Thus, DBS really has two meanings in SAR: (1) the name for SAR invented by Wiley before it was called SAR and (2) the name for a PPI-like mode based on squinted SAR.

In 1952, the University of Illinois demonstrated the SAR concept. In 1953, during a summer study that launched a program known as Project Michigan, ideas related to synthetic apertures were discussed by L. J. Cutrona of the University of Michigan Willow Run Laboratories, C. W. Sherwin of the University of Illinois, W. Hausz of General Electric, and J. Koehler of Philco Corporation.² This resulted in a successful SAR program by the Michigan group.¹³ The Illinois group also demonstrated successful SAR imaging.¹⁴ The work of Cutrona et al.¹³ and Sherwin et al.,¹⁴ plus many other early SAR papers, are compiled in a very useful book by Kovaly.¹⁵ More detailed histories of SAR development are given by Curlander and McConough,⁴ Jackson and Apel,¹⁰ and Ausherman et al.¹¹

17.3 TYPES OF SAR

When we refer to SAR, we usually mean *focused SAR*; the term indicates that the phase information has been optimally processed to produce resolution comparable to the theoretical limit. In the development of SAR, several interesting techniques

preceded the development of focused SAR. These techniques are discussed in order of progressively finer resolution.

Precursors to Focused SAR.

Side-Looking Airborne Radar (SLAR). SLAR consisted of an aircraft-mounted RAR pointed perpendicular to the direction of flight (hence “side-looking”), with crossrange resolution $\sim R\lambda/D$.

Doppler Beam Sharpening (DBS). As previously mentioned, when Wiley first conceived of the concept that we now call SAR, he termed it *doppler beam sharpening*. Wiley explained it as follows: “I had the luck to conceive of the basic idea, which I called Doppler Beam Sharpening (DBS), rather than Synthetic Aperture Radar (SAR). Like all signal processing, there is a dual theory. One is a frequency-domain explanation. This is Doppler Beam Sharpening. If one prefers, one can analyze the system in the time domain instead. This is SAR. The equipment remains the same—just the explanation changes. Conception was reported in a Goodyear Aircraft report in 1951.”¹²

Subsequently, as described in Section 8.1 of Schleher,¹⁶ DBS came to refer to an airborne scanning mode in which the echoes from the scanning real beam are doppler-processed to produce crossrange resolution finer than that provided by the real beam alone; broadside crossrange resolution is $\approx R\lambda/2L_{\text{DBS}}$, where L_{DBS} is the synthetic aperture length generated during a target dwell. Stimson⁵ explains: “Typically, the antenna continuously scans the region of interest...Because the integration time is limited to the length of time a ground patch is in the antenna beam—or, if you prefer, the length of the array that can be synthesized is so limited—the resolution is coarser than can be achieved with a non-scanning antenna” (p. 434).

Unfocused SAR. This type of early SAR is described by Cutrona² as follows: “The coherent signals received at the synthetic array points are integrated, with no attempt made to shift the phases of the signals before integration. This lack of phase adjustment imposes a maximum upon the synthetic antenna length that can be generated. This maximum synthetic antenna length occurs at a given range when the round-trip distance from a radar target to the center of the synthetic array differs by $\lambda/4$ from the round-trip distance between the radar target and the extremities of the array.” Cutrona shows that the crossrange resolution is approximately $\frac{1}{2}(\lambda R)^{1/2}$.

Unfocused SAR is typically not used today and is included here only for historical reasons. It was used in the early days of SAR since the technology of that time did not support focused SAR.

Types of Focused SAR. In focused SAR, a phase correction is made for each returning pulse echo. This essentially results in the theoretical crossrange resolution of Eq. 17.2.

Stripmap SAR. Stripmap SAR (or “strip” SAR) is also sometimes called “search” SAR, since it is useful for imaging large areas at relatively coarse resolution. In stripmap SAR, the beam remains normal to the flight path (the latter is assumed to be a straight line at constant altitude) and continuously observes a *swath* (or *strip*) of terrain parallel to the flight path extending from some minimum range R_{min} to some maximum range R_{max} from the flight path.

For stripmap SAR, the synthetic aperture angle $\Delta\theta$ is essentially equal to the real-aperture beamwidth θ_B :

$$\Delta\theta \approx \theta_B \approx \frac{\lambda}{D} \quad (17.3)$$

Thus

$$\delta_{cr} \approx \frac{\lambda}{2\Delta\theta} \approx \frac{D}{2} \quad (17.4)$$

Under ideal conditions, as long as $D \gg \lambda$ and signal-to-noise ratio (SNR) $\gg 1$, then the smaller the physical antenna, the finer the crossrange resolution, independent of range.

As the physical antenna moves along the synthetic aperture, the return from a point target at a particular range will exhibit a quadratic phase behavior (i.e., phase varies as the square of the time referenced to the closest approach) that is unique to the target's location on the ground.^{2,17} Some stripmap SARs use a filtering approach to take advantage of this phenomenon.¹¹ In fact, for the echo from a point target in the scene, a close analogy exists between its quadratic phase variation during a single pulse (from a linear FM [LFM] pulse echo) and its quadratic phase variation over many pulses due to platform motion (Stimson,⁵ p. 421). Other stripmap SARs divide the strip into *subpatches* and use spotlight-SAR processing (next section) for each subpatch³ (see also Section 4.8 of Ausherman et al.¹¹).

The newer *Range Migration Algorithm* (RMA) (see Chapter 10 of Carrara et al.³), originally developed for seismic applications, provides the most theoretically correct solution to the stripmap image problem. It does not make a far-field approximation but treats the wavefronts as spherical. It is particularly applicable to SAR with very wide fractional bandwidth and/or wide synthetic aperture angle. RMA involves substantial computational complexity; however, as processors become more sophisticated, this limitation is disappearing. A simpler, faster version of RMA is the *Chirp-Scaling Algorithm* (CSA) (see Chapter 11 of Carrara et al.³).

Squinted Stripmap SAR. In this case, the antenna boresight is not normal to the flight path. As seen from a top view, the *squint angle* θ_{sq} is the angle between the antenna boresight and the normal to the flight path; thus, for a broadside beam, $\theta_{sq} = 0$ and $\delta_{cr} \equiv D/2$. More generally,

$$\begin{aligned} \Delta\theta \equiv \theta_B &\equiv \frac{\lambda}{D \cos \theta_{sq}} \\ \delta_{cr} &\equiv \frac{\lambda}{2\Delta\theta} \equiv \frac{D \cos \theta_{sq}}{2} \end{aligned} \quad (17.5)$$

It is assumed here that the synthetic aperture length $L_{SA} \ll R$ and θ_{sq} is essentially constant during a data collection. Depending on details, this condition is valid only for θ_{sq} less than about 45° , since, for a given crossrange resolution, as θ_{sq} increases, L_{SA} increases, and the condition becomes no longer valid.

Spotlight SAR. Spotlight SAR (sometimes called “spot SAR”) is used to obtain a relatively fine-resolution image of a known location or target of interest. As the

platform passes by the target, the beam direction moves to keep pointing at the target. In this way, $\Delta\theta$ may be made considerably greater than θ_B , and δ_{cr} (spotlight) $< \delta_{cr}$ (stripmap). We may wish to make a correction for the variation in received power ($\sim 1/R^4$) as the range to the target varies slightly over the synthetic aperture. This is usually negligible for most spotlight SAR applications but might not be negligible when collection angles are large, such as for the case of foliage-penetration SAR (Section 17.8).

The *synthetic aperture time* t_A required to collect the data for a spotlight SAR image is found as follows:

$$\begin{aligned}\delta_{cr} &\approx \frac{\lambda}{2\Delta\theta} \approx \frac{\lambda R}{2L_{SA} \cos(\theta_{sq})} = \frac{\lambda R}{2Vt_A \cos(\theta_{sq})} \\ t_A &\approx \frac{\lambda R}{2V\delta_{cr} \cos(\theta_{sq})}\end{aligned}\quad (17.6)$$

where V is the platform speed.

Interferometric SAR. Interferometric SAR (InSAR, sometimes also called “IFSAR”) refers to the use of two antennas whose signals are combined coherently. InSAR was originally developed by the Jet Propulsion Laboratory (JPL) to detect ocean currents or moving targets.^{18,19} The two antennas were displaced horizontally on the platform (along a line parallel to the ground) so that the received echoes from a moving target would be different from the corresponding echoes from fixed targets, and thus movers could be detected and analyzed. Later researchers (e.g., Adams et al.²⁰) used two antennas displaced vertically on the platform so that the received echoes from a target above the surface (assumed flat) would be different from the corresponding echoes from a target on the surface, and thus target height could be estimated. Both types of InSAR are discussed in Section 17.8. The former is discussed in “Interferometric SAR for Moving Target Indication (MTI),” and the latter is discussed in “Interferometric SAR for Target Height Measurement.”

Inverse SAR. Skolnik²¹ presents a discussion of Inverse SAR (ISAR). He states, “In SAR, the target is assumed stationary and the radar is in motion. In ISAR, the target motion provides the changes in relative velocity that cause different doppler shifts to occur across the target” (pp. 375–380). Skolnik also includes a discussion of ISAR images of ships obtained by the U. S. Naval Research Laboratory (NRL) (Musman et al.²²). An airborne radar obtains a series of images of a ship that is experiencing pitch/roll/yaw in the waves, and the user is able to identify the ship type and characteristics. Musman et al. discuss feature extraction, multiframe processing, and a capability for automatic target recognition (ATR) of ships. ISAR is also widely used for diagnostic measurements on indoor and outdoor radar cross section (RCS) ranges (Knott et al.,²⁶ p. 516).

Improvements in SAR Resolution. The following example illustrates how SAR crossrange resolution has improved as the preceding types of airborne mapping radar were developed. Let us assume that $\lambda = 0.03$ m (X band), $D =$ aperture diameter = 2 m, $R = 100$ km, $\theta_{sq} = 0$, $V = 180$ m/sec, $L_{DBS} = 10$ m (corresponding to an angular scan rate of 15° sec), and spotlight synthetic aperture length = 5 km ($\Delta\theta \approx 3$ deg).

Then crossrange resolution is approximately as follows for the different modes discussed previously:

SLAR: 1500 m	DBS: 150 m	Unfocused stripmap SAR: 27 m
Stripmap SAR: 1 m	Spotlight SAR: 0.3 m	

17.4 SAR RESOLUTION

In this section, we discuss SAR resolution in more detail. By “resolution,” in keeping with common usage, we mean the precision to which we can measure the location of a point target and not necessarily the ability to resolve two point targets. (For a discussion of this issue, see Wolfe and Zissis.²³) How we do this will be discussed in more detail below.

Since fine range resolution is typically achieved with a single pulse, the corresponding processing is often termed *fast-time processing*. On the other hand, fine crossrange resolution requires multiple pulses, and the corresponding processing is, therefore, often termed *slow-time processing* (Carrara,³ Richards,²⁴ and Klemm²⁵).

Range Resolution. Strictly speaking, SAR refers to a method for improving crossrange resolution, not range resolution. However, because fine range resolution is so necessary to a successful SAR, and also because of an analogy between range and crossrange resolution, we discuss range resolution briefly here.

Fine range resolution is achieved by transmitting and receiving radar waves characterized by a fairly wide bandwidth B . As an example, consider a carrier frequency $f = 10$ GHz and a 10% bandwidth $B = 1$ GHz. One way to achieve this bandwidth (not the best way, in general, but a way that is easy to describe) is to use a *step-frequency* waveform consisting of a series of “single-frequency” pulses, each with a frequency somewhat greater than that of the previous pulse. (By a “single-frequency” pulse, we mean a pulse consisting of a pure sinusoidal tone multiplied by a rectangular function of duration (“width”) τ much longer than the period of the tone. Such a pulse is not truly single-frequency but has a bandwidth of $\approx 1/\tau$. For example, if $\tau = 1$ microsecond, $B(\text{pulse}) = 1$ MHz. This is far less than the bandwidth of the overall step-frequency waveform, equal to the difference between the frequencies of the last and first pulses in the sequence, which is typically hundreds of MHz.)

Step-frequency pulse compression has not proven successful in airborne or spaceborne applications, as compared to the linear-FM (LFM) waveform (see Section 2.6 of Carrara³), and is seldom used. Linear-FM (LFM) is a common waveform used in operational high-power radars, because (1) each pulse contains the full bandwidth, thereby enabling the full bandwidth to be transmitted and received much more quickly than with step-frequency—a great advantage when the radar is moving, such as for SAR—and (2) the hardware is relatively inexpensive and mature. LFM has been successfully employed operationally (e.g., in the U. S. Navy AN/APS-116 and AN/APS-137) since the 1970s. The only apparently successful application of step-frequency has been in ground-based instrumentation radars, where it is less expensive to implement and more time is available for data collection (Knott et al.,²⁶ pp. 35, 540).

Nevertheless, for the moment, we assume the step-frequency waveform because it provides a much simpler example for explaining the principle of range resolution.

Let us assume that the radar transmits a step-frequency waveform consisting of identical groups of pulses, each group consisting of $N (\gg 1)$ “single-frequency” pulses of width τ . Within a pulse group, the frequency of a pulse is Δf greater than that of the previous pulse, and the radar transmits $(PRF)/N$ groups per second, where PRF is the pulse repetition frequency. The waveform bandwidth is $(N - 1) \Delta f \gg 1/\tau$. The phase and amplitude of each pulse echo is digitally recorded by the radar. As shown in Figure 17.1a, a discrete Fourier transform (DFT)—typically a fast-Fourier transform (FFT)²⁷—is applied to this set of N complex samples of frequency-domain data, resulting in a set of N complex numbers in the time-domain corresponding to echoes (magnitude and phase) that would be returned from a very short pulse of width $\approx 1/B$, sampled at time intervals $\Delta t = 1/B$. This is a simple example of pulse compression. Since an incremental delay Δt corresponds to an incremental downrange distance $\Delta r = c\Delta t/2$, we multiply the DFT output by $c/2$ and obtain the echoes corresponding to a set of downrange distances separated by a pixel width of $c\Delta t/2 = c/2B$. Thus, the range resolution (strictly speaking, pixel separation) of a step-frequency waveform of bandwidth B is

$$\delta_r = c/2B \quad (17.7)$$

Although it is beyond the scope of this chapter, it can be shown that such a range resolution of $\approx c/2B$ may be obtained using a wide variety of waveform types, as long as the overall transmitted bandwidth is B . For example, Section 7.2 of Sullivan¹ shows that this is true for the LFM waveform.

Crossrange Resolution. Let us now assume that the airborne (or spaceborne) SAR is observing a scene on the Earth’s surface consisting of a few point targets and that it transmits and receives N identical pulses each of bandwidth B (presumably, though not necessarily, via the LFM waveform) and determines the downrange position of each

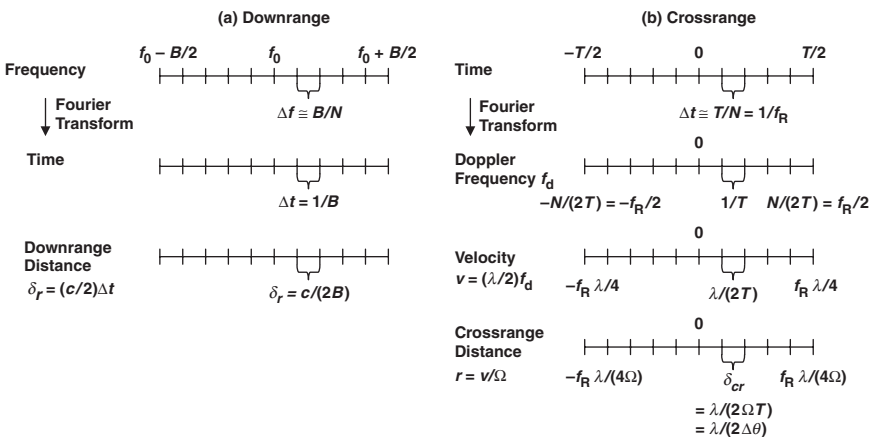


FIGURE 17.1 Range and crossrange resolution: Similar discrete Fourier transform (DFT) processes may be used to obtain range and crossrange resolution.

target with a range resolution of $c/2B$. Let us also assume that the SAR is moving in a straight line at a constant altitude H and constant speed V for a time T along a direction normal to the LOS. The synthetic aperture $L_{SA} = VT$ is assumed small compared with the range R to the center of the target region. As viewed from the target region (also assumed small compared to R), the synthetic aperture subtends the synthetic aperture angle $\approx L_{SA}/R = VT/R$. As the radar moves through its synthetic aperture, it views the scene from slightly different angles. For simplicity, let us assume that during this time the targets do not leave their “range bins” of width $c/2B$. (This assumption will be discussed in Section 17.5, “Range Migration.”)

From the viewpoint of the SAR, the scene appears to be rotating with angular velocity $\Omega = V/R$. During the data collection, the total angle through which the scene appears to rotate is $\Delta\theta = \Omega T = VT/R$. A specific point target appears to have a LOS velocity of Ωr relative to the SAR, where r is the crossrange distance of the target from the LOS. These apparent LOS velocities will result in doppler frequencies (in absolute value) of $2v(\text{apparent})/\lambda = 2\Omega r/\lambda$, where λ is the wavelength corresponding to the carrier frequency.

For each range bin, we now have N complex numbers corresponding to different radar echoes in the time domain. As shown in Figure 17.1b, these N time-domain echoes may be processed using a DFT to produce a set of N frequency-domain returns. The frequency interval between successive returns is $\Delta f = 1/T$, and the overall frequency interval is $(N - 1)/T \approx N/T = \text{PRF} = f_R$. We assume operation at baseband, and thus the frequency in question is the apparent doppler frequency of the targets. We convert this to crossrange by multiplying by $\lambda/2\Omega = \lambda R/2V$:

$$\delta_{cr} \approx \frac{\lambda}{2\Omega T} = \frac{\lambda}{2\Delta\theta} \approx \frac{\lambda R}{2L_{SA}} = \frac{\lambda R}{2VT} \quad (17.8)$$

Note that our assumption that $R \gg VT$ permits the use of small-angle approximations for small $\Delta\theta$. When $\Delta\theta$ is not small, Eq. 17.8 must be appropriately modified.

Summary of SAR Resolution. We have, therefore, now derived the two basic formulas for SAR resolution:

$$\begin{aligned} \delta_r &= c/2B && \text{Range Resolution} \\ \delta_{cr} &= \frac{\lambda}{2\Delta\theta} \approx \frac{\lambda R}{2L_{SA}} && \text{Crossrange Resolution} \end{aligned} \quad (17.9)$$

The processing described produces a two-dimensional array of complex numbers, i.e., each consists of a magnitude and a phase. This ordered array of complex numbers as a function of downrange and crossrange produces a complex radar *image*, i.e., each pixel consists of a magnitude and a phase. Typically the magnitude squared (representing pixel energy) is displayed.

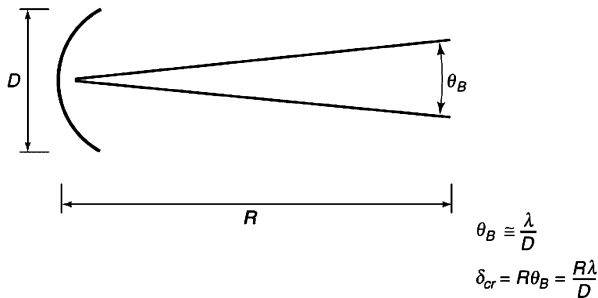
As shown in Chapter 6 of Sullivan,¹ a point target in the scene transforms to a two-dimensional *point-spread function* (PSF) in the radar image, so-called because a point target is displayed in the image as somewhat “spread out.” This PSF is characterized by a *mainlobe* and *sidelobes* in both range and crossrange. Usually *weighting* (also called *tapering* or *apodization*) is applied in the processing, resulting in considerably lower sidelobes, but at the expense of a somewhat broader mainlobe, a price that the user is typically willing to pay. Many types of weighting exist. If no weighting is applied, the PSF is a (*sinc*)² function of the form $(\sin(x)/x)^2$. In that case, the formulas above for SAR resolution

represent the distance from the mainlobe peak to the first null. Note that this definition of SAR resolution is different from the more common definition of the half-power width of the mainlobe. With no weighting, the latter is (0.886) times the values given above; thus the two definitions are not very different. We prefer the former definition because, for no weighting, it results in a simpler formula without the introduction of the factor of (0.886). (More details concerning weighting are given in Section 17.6.)

There are at least two mathematically equivalent ways of considering SAR. As we have developed the concept so far, the crossrange resolution may be considered to result from the doppler shifts resulting from the different apparent line-of-sight velocities of different parts of the scene. However, the crossrange resolution may also be considered to result from the large synthetic aperture, much as fine crossrange resolution would also result from a large real aperture. Per Eq. 17.8, the crossrange resolution (peak-to-first null) of a SAR is finer by a factor of two than the resolution for a RAR of equal aperture. An intuitive explanation for this interesting result is that for RAR, the echo received at a particular aperture location results from energy transmitted from *all locations* in the aperture, whereas for SAR, the echo received at a particular aperture location results from energy transmitted from *that (known) location* in the aperture; i.e., more information is received (Carrara et al.,³ p. 36). Stimson⁵ provides a detailed explanation for this result (pp. 416–417).

Figure 17.2 presents a comparison of RAR and SAR.

Real-Aperture Radar (RAR):
($\lambda = \text{wavelength}$)



Synthetic-Aperture Radar (SAR):

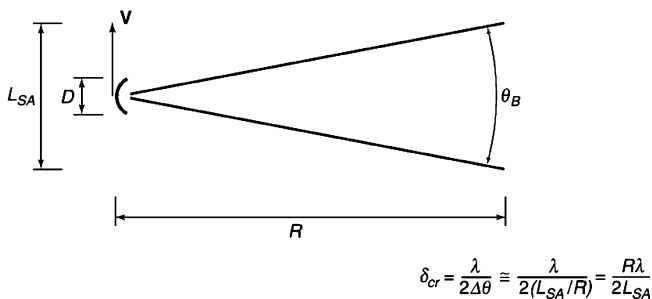


FIGURE 17.2 Comparison of RAR and SAR: The crossrange resolution (peak-to-first-null of antenna pattern) of a SAR is one-half that of a real aperture radar (RAR) of the same aperture diameter. (Courtesy of SciTech Publishing, Inc.)

The sidelobes are also different for RAR and SAR. For a RAR with an unweighted aperture function, the transmitted intensity at the peak of the first angular sidelobe is reduced by -13 dB, and the received intensity from a target in that direction is thus reduced by -26 dB. For a SAR, typically the entire region of the image is in the main beam during the data collection, and there are no effects from the sidelobes of the physical antenna. The sidelobes result solely from the processing, and (with no weighting) the first sidelobe is reduced by -13 dB relative to the main beam.

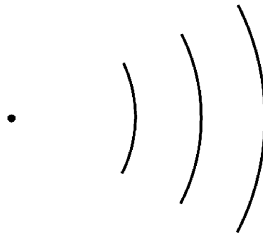
17.5 KEY ASPECTS OF SAR

Range and Velocity Contours. Using fine range resolution, a radar can distinguish between targets at different ranges. A particular target may be determined to be located on a constant-range-contour. In 3D space, these contours are concentric spheres with the radar at the center (Figure 17.3a).

Similarly, using doppler processing, the radar can distinguish between targets of different apparent velocities. If \mathbf{V} is the platform velocity and θ is the angle between \mathbf{V} and the LOS to a stationary target, then the apparent LOS speed of the target is $V_{\text{LOS}} = -V \cos \theta$ (Figure 17.4b). In 3D space, surfaces of constant V_{LOS} are circular cones with axis \mathbf{V} and generating angle θ , with the radar at the vertex. The negative sign occurs

a. Constant-Range Contours:

Concentric Spheres with Radar at Center



b. Constant-Velocity Contours:

Circular Cones with Axis $\hat{\mathbf{V}}$

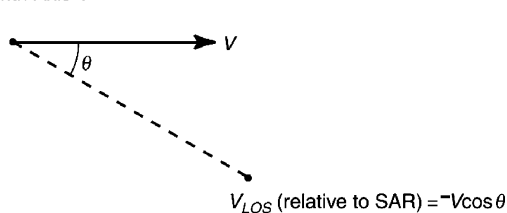


FIGURE 17.3 Range and velocity contours in 3D space: (a) Constant-range contours are concentric spheres with the radar at the center. (b) Constant-apparent-velocity contours are circular cones with the radar at the vertex and the axis along the platform velocity vector. (Courtesy of SciTech Publishing, Inc.)

because we define LOS velocity as dR/dt , where R is the range to the target. Thus, a positive dR/dt corresponds to a receding target and results in a negative doppler frequency shift, and a negative dR/dt corresponds to an incoming target and results in a positive doppler frequency shift.

Consider an airborne radar with an isotropic antenna pattern, with constant velocity along a straight line parallel to a flat ground³ (Figure 17.4a). On the ground, the constant-range contours are the intersections of concentric spheres with the ground—a set of concentric circles with the subradar point at the center (Figure 17.4b). The contours of constant LOS velocity (called *isodops*) correspond to the intersections between the set of cones and the flat ground—a set of nested hyperbolas (Figure 17.4c). Figure 17.4d shows the combination of constant-range circles and the *isodops*. The “nadir line” shown in Figure 17.4 is the locus of subradar points as the platform flies along its path.

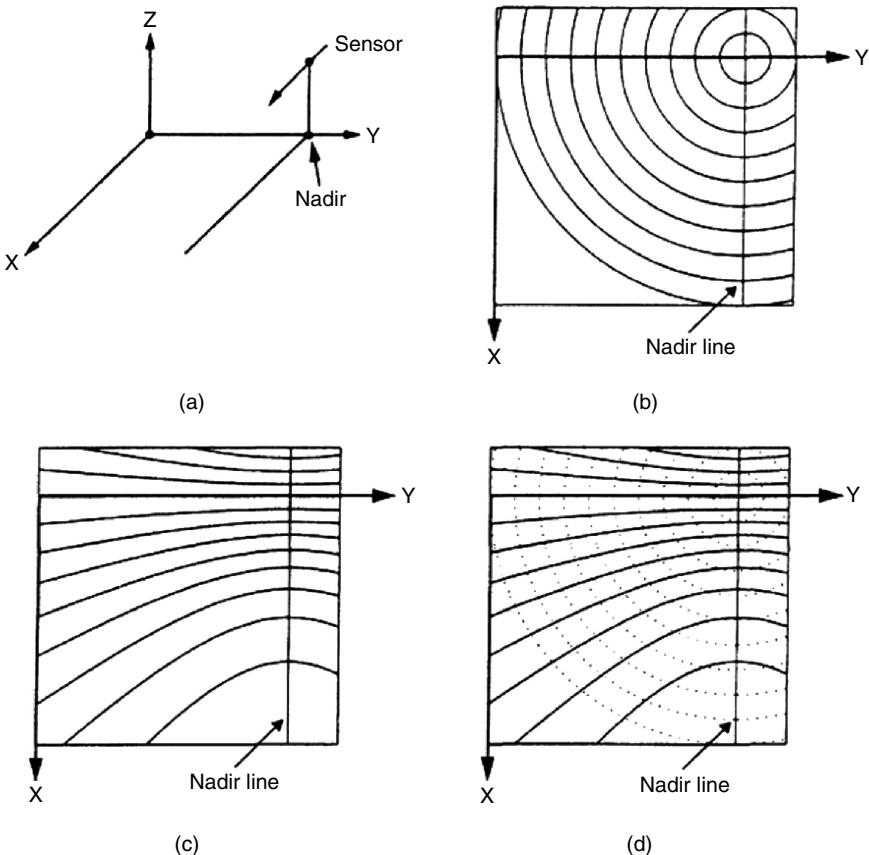


FIGURE 17.4 Range and velocity contours on the Earth's surface: (a) Collection geometry. (b) Constant-range contours are concentric circles with the subradar point at the center; “nadir line” refers to the locus of subradar points. (c) Constant-apparent-velocity contours (“isodops”) are confocal hyperbolas with the axis parallel to the platform velocity vector. (d) Set of intersecting concentric circles and confocal hyperbolas. (Courtesy of SciTech Publishing, Inc.)

Through appropriate range-doppler processing, returns from each intersection cell may be distinguished. Over a small angle about the broadside direction, the range contours and the isodops are essentially orthogonal to each other. The resulting radar returns may be displayed to yield an image of the ground. At a nonzero squint angle, the isodops are not orthogonal to the range contours; however, additional processing corrections can still usually result in an essentially undistorted ground image.

Motion Compensation. The basic theory of SAR relies on the assumption that the platform, and therefore the SAR antenna, is traveling along a straight-line flight path at constant velocity parallel to the ground at constant altitude. This is not exactly true, and for successful SAR imaging, it is necessary that the deviations of the antenna from this nominal flight path be measured, recorded, and compensated for in the processing. This procedure is known as *motion compensation* (sometimes abbreviated *mocomp*). For example, at a particular moment, as a particular frequency is transmitted, if the antenna is estimated to have deviated a distance d away from the nominal flight path along the LOS, the phase correction

$$\Delta\phi = \frac{4\pi d}{\lambda} = \frac{4\pi df}{c} \quad (17.10)$$

with appropriate sign, is added to the measured phase at the frequency f to produce the best estimate of what the recorded phase would have been if the platform had not deviated from the nominal flight path. Similarly, if the platform speed is not constant, the received data are interpolated to produce the best estimate of what they would have been if the speed had been constant.

When the platform is an aircraft, an on-board *Inertial Navigation System (INS)* uses accelerometers and gyroscopes to measure the deviations. Sometimes a smaller *Inertial Measurement Unit (IMU)* relying on the same general principles is “strapped down” very near the antenna. Without an absolute reference frame, the outputs of any INS or IMU will drift with time as errors accumulate. An absolute frame for position and velocity may be obtained from the *global positioning system (GPS)*, a constellation of at least 24 satellites in polar Earth orbit providing continuous reference signals for determination of precise position and velocity.²⁸

Slant and Ground Planes. When a SAR image is initially produced, the range pixel size δ_r is usually a constant. (It is generally chosen to be somewhat less than $c/2B$, e.g., $0.75(c/2B)$, to ensure adequate sampling). As illustrated in Figure 17.5, the actual ground locations that correspond to these range samples are not spaced at constant intervals in ground range. Near the scene center, they are spaced at

$$\delta_g \equiv \delta_r / \cos \psi \quad (17.11)$$

where ψ is the grazing angle. At ground ranges closer to the radar, they are spaced still farther apart because of the spherical range contours. Near the scene center, the image corresponds to the projection of the ground onto a *slant plane*; this plane is determined by the LOS and its perpendicular in the ground plane. We often refer to this type of image as a *slant-plane image*. By appropriate interpolation and resampling, a *ground-plane image* with $\delta_g = \text{constant} = \delta_{cr}$ may be produced. Ground-plane imagery with minimal distortion is necessary if comparison is to be made with maps or with imaging taken from other sensors, such as optical sensors or other SARs.

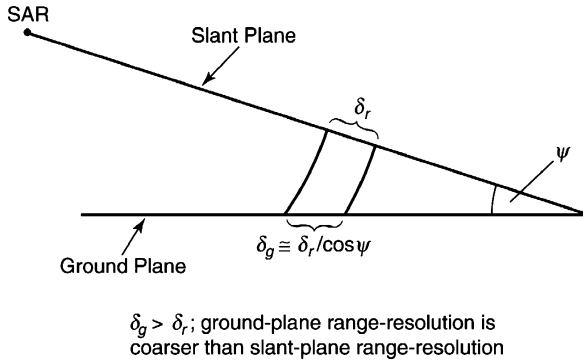


FIGURE 17.5 Slant and ground planes: The slant plane is determined by the radar line-of-sight and its perpendicular in the ground plane. Ground-plane range resolution is coarser than slant-plane range resolution. (Courtesy of SciTech Publishing, Inc.)

Pulse Repetition Frequency (PRF) Requirements for SAR. For broadside operation, the apparent angular velocity of the scene rotation is

$$\Omega = \frac{V}{R} \quad (17.12)$$

With respect to the radar, the relative velocity of point A (see Figure 17.6) at the first null of the main beam is

$$v_A = -\Omega r = -\left(\frac{V}{R}\right)\left(\frac{\lambda R}{2D}\right) = -\frac{\lambda V}{2D} \quad (17.13)$$

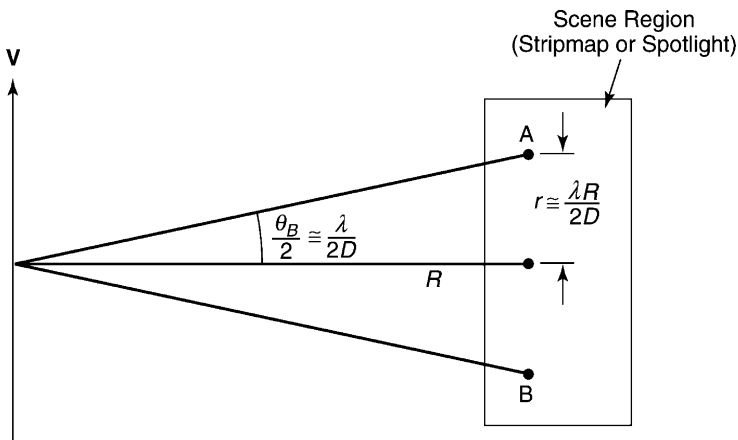


FIGURE 17.6 Minimum PRF for SAR: The apparent line-of-sight velocity of point A is toward the radar, whereas the apparent line-of-sight velocity of point B is away from the radar. These determine the minimum PRF of $2V/D$, where V = platform speed and D = antenna physical diameter. (Courtesy of SciTech Publishing, Inc.)

Similarly, the relative velocity of point B on the opposite side of the beam is

$$v_B = \Omega r = \left(\frac{V}{R}\right)\left(\frac{\lambda R}{2D}\right) = \frac{\lambda V}{2D} \quad (17.14)$$

Thus, the range of relative velocities in the scene is

$$\Delta v = \Omega r - (-\Omega r) = 2\Omega r = \frac{\lambda V}{D} \quad (17.15)$$

The range of doppler frequencies received from the scene is

$$\Delta f_d = \frac{2}{\lambda} \frac{\lambda V}{D} = \frac{2V}{D} \quad (17.16)$$

Thus, to avoid velocity ambiguity, the PRF must be at least $2V/D$. Writing

$$f_R(\min) = \frac{2V}{D} = \frac{1}{t_R(\max)} \quad (17.17)$$

we have

$$V t_R(\max) = \frac{D}{2} \quad (17.18)$$

Thus, the distance traveled by the platform during the time between pulses (t_R) must be no more than $D/2$, and the SAR must transmit at least two pulses as its physical antenna passes a stationary point in space.

We also frequently want range-unambiguous operation, which implies

$$\frac{2V}{D} \leq f_R < \frac{c}{2R} \quad (17.19)$$

For example, if $V = 180$ m/s (≈ 350 kts), $D = 2$ m, and $R = 150$ km, then $180 \text{ Hz} < f_R < 1000 \text{ Hz}$.

Eq. 17.19 is really two equations. We use $<$ for the second equation instead of \leq because when the equality is used, a pulse is being transmitted just as the echo from the previous pulse is being received, resulting in eclipsing and consequent loss of the received information.

Skolnik²¹(pp. 520–521) points out that, since for stripmap SAR the crossrange resolution $\delta_{cr} \cong D/2$ (Eq. 17.4), Eq. 17.19 becomes

$$\frac{V}{\delta_{cr}} \leq f_R < \frac{c}{2R} \quad (17.20)$$

This leads to the condition

$$\frac{R}{\delta_{cr}} \leq \frac{c}{2V} \quad (17.21)$$

Thus, the unambiguous range R_u and the resolution of a stripmap SAR cannot be selected independently of one another. Skolnik further points out, quoting Bayma and McInnes,²⁹ that more sophisticated reasoning leads to the condition

$$\frac{R_u}{\delta_{cr}} \leq \frac{c}{4.7V} \quad (17.22)$$

Skolnik²¹ continues, “When a SAR images the ground from an elevated platform, the unambiguous range can correspond to the distance between the forward edge and the far edge of the region to be mapped. This requires that the elevation beamwidth be tailored to illuminate only the swath S that is to be imaged by the radar. The swath S is often much smaller than the maximum range so that the PRF can be increased to allow the unambiguous range R_u to encompass the distance $S \cos \psi$, where ψ is the grazing angle” (p. 521). For a stripmap SAR, Eq. 17.22 then becomes

$$\frac{S}{\delta_{cr}} \leq \frac{c}{(4.7)V \cos \psi} \quad (17.23)$$

Range Migration. As we have seen, a SAR may obtain range resolution of $\delta_r = c/2B$, where B = signal bandwidth, and obtain cross-range resolution through doppler processing, with $\delta_{cr} = \lambda/2\Delta\theta$. If we wish to prevent *range migration* (movement of a point target from one range bin to the next during the time required to collect the data for image formation), we would require that ΔR , the variation of range during the data collection (over the synthetic aperture), be less than δ_r .

We consider the formation of a SAR image after collecting data over an aperture time t_A . The SAR flight path is a straight line at constant speed and altitude over a flat ground. From Levanon¹⁷ we have

$$R_{\max} \equiv R_0 + \frac{V^2(t_A/2)^2}{2R_0}, \quad R_{\min} = R_0 \quad (17.24)$$

where R_0 = distance from the radar to the scene center in the middle of the data collection interval, and R_{\max} = distance from the radar to the scene center at the beginning and end of the data collection interval. Then

$$\Delta R = R_{\max} - R_{\min} = \frac{(Vt_A)^2}{8R_0} = \frac{L_{SA}^2}{8R_0} = \frac{R_0(\Delta\theta)^2}{8} = \frac{R_0\lambda^2}{32\delta_{cr}^2} < \delta_r \quad (17.25)$$

The last inequality is necessary for the condition of no range migration. For example, parameters for a SAR might be $R_0 = 200$ km, $\lambda = 0.03$ m, and $\delta_r = \delta_{cr} = 1$ m; then, $\Delta R = 5.6$ m $> \delta_r$, and the condition is not satisfied. Thus, *the processor must usually correct for range migration*. However, this is typically accomplished by modern SAR processing methods.³ For spotlight SAR, the *polar format algorithm*^{3,11} is often used to accomplish this correction.

Other Processing Functions. Curlander et al.⁴ provide a detailed discussion of several key options for SAR processing beyond simple image formation.

- *Clutterlock* (Curlander et al.,⁴ Chapter 5) refers to the use of information in the received signals to ascertain the center frequency of the echoes from the ground (clutter) and compensate for sideways drift of the platform.
- *Autofocus* (Curlander et al.,⁴ Chapter 5) describes the use of information in the (complex) image itself to estimate and correct phase errors, and then reprocess and sharpen the image (see also Carrara et al.³).
- *Calibration* (Curlander et al.,⁴ Chapter 7) refers to the use of targets of known radar cross section (RCS) in the scene to obtain the absolute level of RCS per pixel and thus σ^0 , the ground RCS per unit area.
- *Geolocation* (Curlander et al.,⁴ Chapter 8) is the process of determining the absolute latitude and longitude of pixels in the SAR image, typically using information from the GPS.

17.6 SAR IMAGE QUALITY

It is clearly important for a SAR to produce high-quality imagery. Image quality is typically measured using several *image-quality metrics* (IQMs) described in the following sections. More detailed discussion of SAR imagery is given by Henderson and Lewis³⁰ and Oliver and Quegan.³¹

Point-Spread Function (PSF). A point target may be considered an impulse input to a SAR processor, and the PSF in the image may be regarded as an impulse response (IPR). The primary IQM for most SARs is the width (meters) of the PSF mainlobe at its “half-power points,” or points where the intensity (power, proportional to voltage squared) is one half, or -3 dB, relative to the mainlobe peak. This IQM is typically referred to as the “3-dB width.”

To obtain fine resolution in either range or crossrange, a Fourier transform (FT) is performed on a set of collected data. Since all data samples have essentially the same magnitude, for either range or crossrange we essentially perform a FT on a rectangular function, which produces a $(\text{sinc})^2$ function $(\sin(x)/x)^2$, with a 3-dB width of $(0.886)\delta_{\text{pn}}$ (where δ_{pn} = peak-to-first-null interval) and a first sidelobe -13.3 dB below the peak.

As mentioned in Section 17.4, when a tapering, or weighting, function multiplies the rectangular input, the result is typically a function with broader mainlobe and lower sidelobes than the $(\text{sinc})^2$ (see Section 2.2.2 of Sullivan¹). A typical weighting function used in SAR processing is Taylor weighting, with the first sidelobe constrained to be -35 dB below the peak and “nbar = 5” (see Section D.2 of Carrara et al³), which produces a widened main beam of 3-dB IPR value $(1.19)\delta_{\text{pn}}$. Another choice is Hann¹⁷ (or “Hanning”³) weighting, which results in an even wider main beam of $(1.43)\delta_{\text{pn}}$; the first sidelobe is -31.7 dB below the peak, and the far sidelobes are very low compared with uniform or Taylor weighting. An excellent discussion of over 20 weighting functions (not including Taylor) is given by Harris.³²

Signal-To-Noise Ratio (SNR). For a real radar, for which the exact phase of the target echo can never be known in advance, the greatest achievable signal-to-noise ratio (SNR) is (Sullivan,¹ Section 4.2.2)

$$\text{SNR} = \frac{E}{kT_0F} \quad (17.26)$$

$$E = P_{\text{Rx-avg}} t_A \quad (17.27)$$

where E = collected energy; k = Boltzmann’s constant = 1.38×10^{-23} joule/Kelvin; T_0 = standard temperature (290 K); F = “noise figure,” which is typically about 2; $P_{\text{Rx-avg}}$ = average received power; and t_A = time to form the synthetic aperture. (The denominator of Eq. 17.26 is correct only if the temperature of the radar is the same as that of the scene, which we assume; see Chapter 2 and Section 1.11 of Sullivan¹):

$$E = \frac{P_{\text{Tx-avg}} G^2 \lambda^2 \sigma}{(4\pi)^3 R^4 (\text{Loss})} \cdot t_A = \frac{P_{\text{Tx-avg}} A^2 \eta^2 \sigma}{4\pi R^4 \lambda^2 (\text{Loss})} \cdot t_A \quad (17.28)$$

where $P_{\text{Tx-avg}}$ = average transmitted power, G = antenna gain, σ = target radar cross section (RCS), A = antenna aperture area, η = antenna efficiency, and the radar losses are represented by (Loss) .

For SAR, at $\theta_{\text{sq}} = 0$, from Eq. 17.6,

$$t_A = \frac{\lambda R}{2V\delta_{\text{cr}}} \quad (17.29)$$

Thus

$$\text{SNR} = \frac{P_{\text{Tx-avg}} G^2 \lambda^3 \sigma}{2(4\pi)^3 R^3 k T_0 F(\text{Loss}) V \delta_{\text{cr}}} = \frac{P_{\text{Tx-avg}} A^2 \eta^2 \sigma}{8\pi R^3 \lambda k T_0 F(\text{Loss}) V \delta_{\text{cr}}} \quad (17.30)$$

If a flat ground is being observed, then

$$\sigma = \sigma^0 \delta_{\text{cr}} \delta_r / \cos \psi \quad (17.31)$$

where σ^0 characterizes the ground RCS per unit area and δ_r = pixel width in slant range. Then the signal-to-noise ratio (SNR) is

$$\text{SNR} = \frac{P_{\text{Tx-avg}} G^2 \lambda^3 \sigma^0 \delta_r}{2(4\pi)^3 R^3 k T_0 F(\text{Loss}) V \cos \psi} = \frac{P_{\text{Tx-avg}} A^2 \eta^2 \sigma^0 \delta_r}{8\pi R^3 \lambda k T_0 F(\text{Loss}) V \cos \psi} \quad (17.32)$$

This agrees with Skolnik,²¹ Eq. 14.15, and Curlander et al.,⁴ Eq. 2.88.

It is very useful to consider the *noise-equivalent sigma-zero* ($NE\sigma^0$), defined as the level of σ^0 that produces a received power equal to the thermal noise power, i.e., an SNR of unity. We set $\text{SNR} = 1$ and have

$$NE\sigma^0 = \frac{2(4\pi)^3 R^3 k T_0 F(\text{Loss}) V \cos \psi}{P_{\text{Tx-avg}} G^2 \lambda^3 \delta_r} = \frac{8\pi R^3 \lambda k T_0 F(\text{Loss}) V \cos \psi}{P_{\text{Tx-avg}} A^2 \eta^2 \delta_r} \quad (17.33)$$

For example, if $R = 200$ km, $T_0 = 290$ K, $F = 2$, $\text{Loss} = 5$, $V = 180$ m/s, $\psi = 10^\circ$, $P_{\text{avg}} = 700$ W, $G = 34$ dB, $\lambda = 0.03$ m (X band), and $\delta_r = 0.3$ m, then $NE\sigma^0 = -22$ dB.

A clear SAR image must have an SNR greater than about 5 dB. From Barton³³ and summarized in Section 3.2 of Sullivan,¹ we see that this example SAR could image “wooded hills,” i.e., $\sigma^0 \approx -17$ dB, with $\text{SNR} \approx 5$ dB, but could not image “flatland” (perhaps desert) at $\sigma^0 \approx -27$ dB, since $\text{SNR} \approx -5$ dB.

Integrated Sidelobe Ratio (ISLR). An actual PSF typically resembles the theoretical PSF but is somewhat different from it, especially in the sidelobes, due to phase noise, motion compensation imperfections, and other “real-world” effects. A useful figure of merit is the integrated sidelobe ratio (ISLR), defined as³

$$\text{ISLR} = \frac{\text{Integral over PSF Sidelobes}}{\text{Integral over PSF Mainlobe}} \quad (17.34)$$

ISLR is usually measured in dB; a typical value might be -20 dB. Low ISLR is clearly desired.

Multiplicative Noise Ratio (MNR). Thermal noise (generally internal when the radar is a SAR) is often referred to as *additive noise*, since it adds to the scene independent of the scene content. Another type of unwanted background in a SAR image

is often called *multiplicative noise* (not really noise in the strict sense), which is proportional to the average scene intensity.

Carrara et al.³ define multiplicative noise as follows: “The principal contributors to multiplicative noise are the integrated sidelobes of the system impulse response, the energy present in the scene as a result of range and azimuth ambiguities, and digital [i.e., from quantization in the analog-to-digital converter] noise” (p. 332).

The *multiplicative noise ratio (MNR)*³ of a SAR image is defined as the ratio of the image intensity in *no-return area (NRA)* (not including thermal noise) divided by the average image intensity in a relatively bright surrounding area (in principle not including thermal noise). An NRA is an area with essentially zero return—for example, a shadow area, a very smooth area such as a calm lake, or a specially constructed large sheet of aluminum.

Another, similar SAR image quality metric (IQM) is the *contrast ratio (CR)*, defined as the ratio of the average intensity of a typical bright region in a SAR image to the intensity of an NRA. If thermal noise is negligible, then $CR = 1/MNR$.

Comparison of SAR Imagery and Optical Imagery. The human eye is, of course, a system for producing images using visible light. The light hits the lens and is focused upon the retina, and the resulting image is transmitted to the brain. Over many millennia, humans have become fully accustomed to seeing and processing this visible imagery. Therefore, upon seeing a SAR image, we may instinctively assume that it has certain properties of a visible image, which, in fact, it does not possess. Optical imagery is based on an “angle-angle” principle, whereas SAR imagery is based on a very different “range-crossrange” principle.

The top illustration in Figure 17.7 illustrates the appearance of a flat landscape to the human eye (or a camera). The terrain is illuminated by sunlight, at least partially diffused through the atmosphere. At the eye, each pixel subtends the same azimuth and elevation angles. Thus, pixels farther from the eye are larger (coarser resolution), in both downrange and crossrange, than pixels closer to the eye.

The bottom illustration in Figure 17.7 shows that, for a SAR image, the situation is quite different (assuming adequate SNR). The range pixel size δ_r is

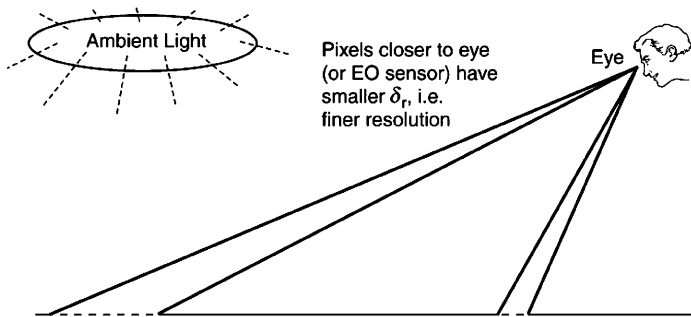
$$\delta_r \equiv \frac{c}{2B} \cdot \frac{1}{\cos \psi} \quad (17.35)$$

Pixels farther from the SAR are smaller in range (smaller grazing angle and finer downrange resolution) than pixels closer to the SAR; and crossrange resolution is independent of range.

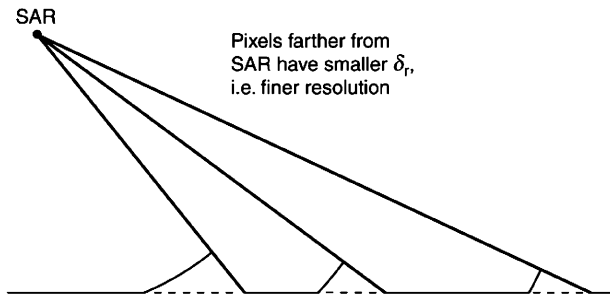
When we display a SAR image, especially of a large landscape, it is usually most satisfying to display it with the SAR direction at the top. The finer resolution pixels are at the bottom, just as they are with a naturally oriented optical image. This orientation tends to look most natural to a human observer.

Because SAR imagery and optical imagery are collected using entirely different physical principles, we should not be surprised if they look different. A good example of this is provided in a SAR image of the Washington Monument, courtesy of the Environmental Research Institute of Michigan, now General Dynamics, Ypsilanti, MI. The top illustration in Figure 17.8 illustrates the collection geometry (and the schematic result) of optical imagery of the Washington Monument with the Monument’s shadow pointed toward the observer. We assume that the sun is to the south of the Monument and the observer is to the north. The image shows a shadow on the north

Optical Image of Terrain



SAR Image of Terrain



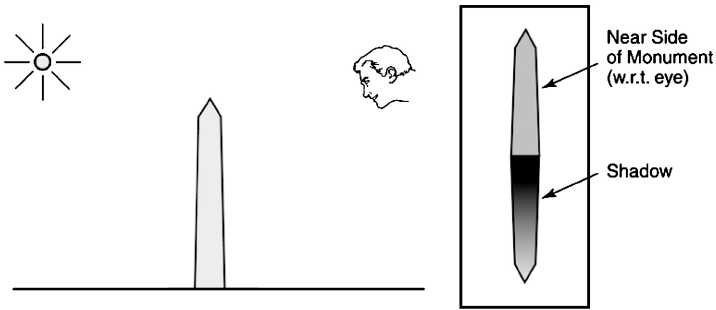
"Natural" direction for viewing image is with SAR at top

FIGURE 17.7 Comparison of SAR and optical imagery: Optical imagery is based on an "angle-angle" principle. SAR imagery is based on a "range-crossrange" principle. Often optical and SAR images of the same target region do not look the same to a human observer. (Courtesy of SciTech Publishing, Inc.)

side cast by the sun. The portion of the Monument visible in the image is the north side, illuminated by diffusely scattered sunlight. In comparison, the bottom illustration in Figure 17.8 shows the geometry and result of SAR imagery, again with the shadow on the north side. This time the shadow is cast by the SAR itself. The portion of the monument visible in the image is the *south* side. Figure 17.9 shows the SAR image. It does not look entirely like an optical image, nor should it.

Another difference between SAR and optical images is the presence of *speckle* (see Section 2-5.1 in Henderson and Lewis³⁰) in the former. Let us consider a particular pixel of a complex image of complicated terrain, such as vegetation. (By "pixel" we mean the complex number—magnitude and phase—that, after SAR processing, corresponds to a particular location on the ground.) If only one scatterer were in the region of ground represented by the pixel, then the pixel magnitude and phase would be a function of the scatterer's exact position. Since the region represented by the pixel typically contains many scatterers, the complex pixel value is the sum of the

Optical Image of Washington Monument



SAR Image of Washington Monument

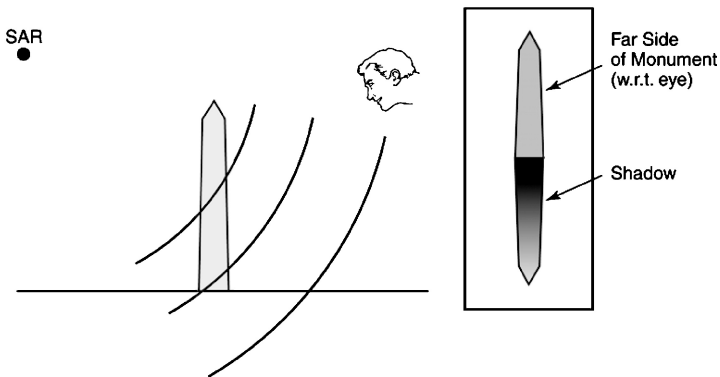


FIGURE 17.8 Principles of imaging the Washington Monument: For the geometry shown, the optical image shows the side of the Monument on the same side as the shadow, whereas the SAR image shows the side of the Monument on the opposite side of the shadow. (Courtesy of SciTech Publishing, Inc.)

complex numbers that each results from one of the scatterers. Thus, when terrain, especially vegetation, is imaged, the amplitude (voltage) of a particular pixel is the magnitude of the complex sum of the coherent returns from many scatterers within the pixel. In another nearby pixel, even if the terrain is nominally the same as in the first pixel, the coherent returns will add differently and the pixel magnitude will be somewhat different. This phenomenon, characteristic of coherent imagery, causes SAR imagery of terrain to exhibit more pixel-to-pixel fluctuation (speckle) than corresponding optical imagery.

Stimson⁵ points out, “Sometimes the beam of the real antenna may be wide enough to enable the same area to be mapped several times without changing the antenna’s look angle. This is called *multilook mapping*. When the maps are superimposed (i.e., when [the magnitudes of] successive returns from each resolution cell are averaged), the effects of scintillation [i.e., speckle] are reduced” (p. 432).



FIGURE 17.9 SAR image of the Washington Monument: The SAR image shows the side of the Monument that is on the opposite side of the shadow, which may appear counterintuitive to a human observer. (Courtesy of General Dynamics, Ypsilanti, Michigan)

17.7 SUMMARY OF KEY SAR EQUATIONS

A review of the basic equations of SAR follows:

- Range resolution = $\delta_r \cong c/2B$ (c = speed of light, B = pulse bandwidth)
- Crossrange resolution = $\delta_{cr} \cong \lambda/2\Delta\theta$
(λ = wavelength, $\Delta\theta$ = angle subtended by synthetic aperture)
- Physical beamwidth $\cong \lambda/D$ (D = antenna diameter)

- Crossrange resolution for stripmap SAR:

$$\delta_{cr} \approx \frac{\lambda}{2\Delta\theta} \approx \frac{\lambda}{2(\lambda/D)} = \frac{D}{2} \quad (17.36)$$

- Image Collection Time: $t_A = \lambda R / (2V\delta_{cr}\cos\theta_{sq})$
- PRF: $f_R = PRF \geq 2V/D$ (V = platform velocity)
- PRF limits for unambiguous range, $f_R < c/2R$:

$$\frac{2V}{D} \leq f_R < \frac{c}{2R} \quad (17.37)$$

$$\text{For stripmap SAR, } \frac{S}{\delta_{cr}} \leq \frac{c}{(4.7)V\cos\psi} \quad (17.38)$$

- Signal-to-noise ratio:

$$SNR = \frac{P_{Tx-avg} G^2 \lambda^3 \sigma^0 \delta_r}{2(4\pi)^3 R^3 k T_0 F(\text{Loss}) V \cos\psi} = \frac{P_{Tx-avg} A^2 \eta^2 \sigma^0 \delta_r}{8\pi R^3 \lambda k T_0 F(\text{Loss}) V \cos\psi} \quad (17.39)$$

17.8 SPECIAL SAR APPLICATIONS

In this section, we briefly discuss several specific aspects of SAR, specifically polarimetric SAR, moving targets, vibrating targets, measurement of object height, and foliage-penetration SAR.

Polarimetric SAR. Usually when a radar transmits a pulse at a particular polarization (e.g., horizontal—H), it receives the echoes at the same polarization. Some radars are capable of transmitting at one polarization and receiving at two orthogonal polarizations (e.g., horizontal [H] and vertical [V] or right-circular [R] and left-circular [L]). Furthermore, some radars can transmit at either of two orthogonal polarizations and receive at either of the transmitted polarizations; and the choice of transmitted and received polarizations can be varied from pulse to pulse. If the phases as well as the magnitudes of the echoes are obtained, then such a radar is fully *polarimetric*. We may designate the choice of polarizations as follows: HV is “transmit H, receive V,” and so forth.

Fully polarimetric SARs have been demonstrated (Sullivan et al.³⁴ and Held et al.³⁵). For example, Sullivan et al.³⁴ includes HH and HV X-band SAR images taken of the same scene at the same time using HH and HV modes interleaved on a pulse-to-pulse basis. The SAR described could, using pulse-to-pulse interleaving, transmit/receive first HH, then HV, then VH, and then VV data, and produce four corresponding simultaneously collected complex images, such that the phases of the corresponding pixels in the four images bear a specific relationship to each other, depending on the target type.

Novak et al.³⁶ developed an optimal *polarimetric whitening filter* for enhanced target detection in such sets of fully-polarimetric SAR images. Using fully polarimetric data from a 33-GHz SAR, they showed that dihedral reflectors look quite different from trihedral reflectors in fully-polarimetric SAR imagery. Few dihedrals exist in K_a -band natural clutter; thus, if a portion of a SAR image corresponds closely to a dihedral, then the region is likely to contain cultural (human-made) object(s).³⁷

Moving Targets in a SAR Image.

Displacement of a Moving Target. The basic theory of SAR assumes that the ground (scene) is stationary. A moving target in the scene will have a “wrong” relationship between its location and its line-of-sight velocity. If the target motion is in a straight line at constant speed, the target image will be displaced in crossrange by

$$r_{\text{displ}} = \frac{V_{\text{LOS}}}{\Omega} = \frac{V_{\text{LOS}} R}{V} \quad (17.40)$$

where Ω is the apparent rotation rate of the scene relative to the radar and V_{LOS} is the target velocity component along the radar line-of-sight. In general, complicated motion of a target during a SAR data collection prevents formation of a clear SAR image of the target.

Detection of Moving Targets in SAR Images. Various processing methods have been developed to detect and reposition moving targets:

Single-Aperture Moving-Target Indication (MTI) SAR With respect to conventional single-aperture SAR, key results have been obtained by several authors, including Raney,³⁸ Freeman,³⁹ Freeman and Currie,⁴⁰ and Werness et al.⁴¹ If the PRF is greater than the minimum necessary to produce a SAR image, then further doppler bands are available. These bands can be used for additional information, and processing results for moving targets will be different from those for fixed targets. Freeman³⁹ presents a summary of potential results for moving targets, covering such issues as azimuth shift, range walk, and azimuth defocus: “Probably the worst defect...will be displacement of moving targets in the azimuth direction, away from their true position on the ground. The prefilter we have described is optimised for targets traveling radially...Such targets will appear at their correct position in the MTI image.”

Interferometric SAR (InSAR) for Moving Target Indication (MTI) As mentioned in Section 17.3, Interferometric SAR (InSAR, sometimes also called IFSAR) refers to the use of two antennas whose signals are combined coherently. The two antennas are displaced horizontally (along a line parallel to the ground) to detect and analyze moving targets and are displaced vertically to estimate terrain height. Both types of InSAR are discussed herein. The former is discussed in this section and the latter is discussed later in “Interferometric SAR (InSAR) for Target Height Measurement.”

InSAR to detect moving targets was originally developed by the Jet Propulsion Laboratory (JPL) to detect ocean currents,^{18,19} and has been improved by several authors.⁴² One of the most sophisticated techniques has been developed for the Joint STARS aircraft and uses an interesting combination of SAR and MTI techniques to detect and evaluate moving targets.²¹

The Joint STARS SAR mode involves a classical single-receiver-channel spotlight SAR that dwells on a designated ground-referenced coordinate for a duration that results in a nominally square point-spread function (i.e., downrange resolution = crossrange resolution). The MTI mode is capable of detecting and accurately geolocating both exoclutler (i.e., target moving faster than apparent terrain motion) and endoclutler (i.e., target moving more slowly than apparent terrain motion) returns from moving targets that, in general, have radar cross sections that are smaller than

the corresponding main-beam clutter-only cells. It accomplishes this by transmitting a coherent burst of pulses that are subsequently received by each of three linearly displaced subarrays (or interferometer ports). In each channel, the pulses are fast-time and slow-time processed into a set of range and doppler cells whose intensities may be considered as a SAR image of the scene (although not as fine in range or doppler resolution as in the SAR mode and generally not with a nominally square PSF). Each of the interferometer ports produces a (complex-valued) range-doppler “image” that could be called a “SAR” image, since it was formed from a coherent sequence of pulses, and the subsequent complex pair-wise combining of these images with the proper relative complex weighting to null the clutter can be considered as an InSAR process. On the other hand, to avoid confusion with the type of interferometric SAR that is used for target height measurement, the Joint STARS team typically refers to their process as “Clutter Suppression Interferometry” or simply “CSI”.[‡]

Barbarossa and Farina⁴³ show that, by using multiple subapertures, detection and repositioning of moving targets can be considerably improved, in an extension of the real-beam Displaced Phase-Center Antenna (DPCA) technique (Staudaher⁴⁴). They developed a procedure for SAR processing using an arbitrary number of subapertures, separated horizontally, to cancel ground clutter and image a moving target. Their approach is a combination of space-time processing (see the literature^{1,25,45,46} for a discussion of Space-Time Adaptive Processing or STAP) and time-frequency processing.^{47,48} Figure 17.10a shows a simulated point-spread function (PSF) of a moving point target after clutter cancellation, and Figure 10b shows the final simulated PSF after range migration compensation.

The authors state: “The [point] target is supposed moving on the terrain (shadowing effects have been neglected) at a constant velocity, in a direction oblique with respect to the radar motion. The velocity parameters have been chosen in order to make evident the presence of range migration and of cross-range smearing of the target image. The ground reflectivity has been assumed equal to the target reflectivity (this is quite a pessimistic assumption, because in many cases of practical interest, the target reflectivity is higher). A receiver thermal noise, 40 dB below the target return, has also been summed to the received signal. The ground echo is first canceled, by using a two-element antenna and two time samples. . . The two antennas are separated by $d = vT$. [v = platform speed, T = pulse repetition interval.] A SAR image is then formed by conventional techniques. The result is shown in Figure [17.10a]. The smearing of the moving pointlike target is evident. Given the motion parameters, the target has migrated over six range cells. This is the cause for the broadening of the target image even in range, as well as in cross range. . . The target echo causes a detection and initializes the motion estimation channel. The high [fine] resolution data are initially smoothed in range to decrease [coarsen] the range resolution. Then the processor looks for the range cell with the maximum energy content and computes the WVD [Wigner-Ville Distribution⁴⁸] of that cell only. . . The phase history is then used for compensating the range migration and the phase shift on the high [fine] resolution range data. The final image is shown in Figure [17.10b]. The sharpening of the target image is quite evident.” Barbarossa and Farina assumed a point target in their simulation. They obtain a precise location of a simulated moving point target, but do not claim to have produced a simulated image of an extended moving target, such as a vehicle.

[‡] Paragraph courtesy of Dr. Marshall Greenspan, Northrop-Grumman Corporation.

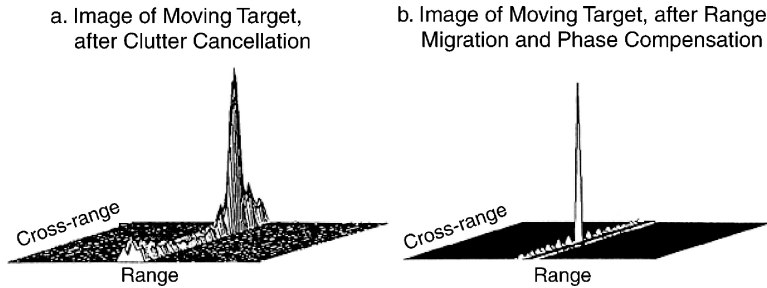


FIGURE 17.10 SAR image of a moving target using multiple subapertures for clutter cancellation (simulated data): (a) adaptive processing and (b) adaptive processing plus SAR (after S. Barbarossa and A. Farina⁴³ © IEEE 1994)

Guarino and Ibsen⁴⁹ describe an experiment using the AN/APG-76 radar. “The radar provides a unique simultaneous SAR/GMTI [Ground Moving Target Indication—scanning real aperture radar] mode in which detected targets are displayed on the SAR map as moving target symbols. The symbols are accurately located at their true azimuth position relative to the map center...The [SAR] map on which the moving target symbol is displayed is collected and processed simultaneously with the GMTI.” The authors also make clear that Global Positioning System (GPS) inputs were essential to their accurate location of targets; fixed targets were geolocated to an absolute accuracy of better than 3 meters, and moving target vehicles to an absolute accuracy of about 15 meters. Stimson⁵ also discusses these AN/APG-76 results (pp. 434, 554).

Imaging of Moving Targets in SAR Images. Perry et al.⁵⁰ have developed a method for SAR imaging of ground-moving targets that have unknown straight-line, constant-speed motion. They process the received phase history with a “keystone formatting” procedure that eliminates the effects of linear range migration for all ground-moving targets, regardless of their unknown velocity. The processing procedure then automatically focuses the moving targets. Figure 17.11a shows a conventionally processed SAR image containing three moving targets—a military truck (type M813), a tractor-trailer truck, and a surrogate (i.e., a full-size replica) of a missile transporter-erector-launcher (TEL). Figure 17.11b shows the focused image of the tractor-trailer resulting from the processing. The two-foot resolution clearly shows the outline of the cab and trailer of the truck.

Vibrating Targets in a SAR Image. Consider a SAR observing a scene that contains a point target whose position is oscillating sinusoidally (vibrating) (see Section 9.4 of Carrara et al.³). The component of the vibration amplitude that is parallel to the line-of-sight (LOS) is d . The variable component of the radar-target distance is then

$$\Delta R_{\text{tgt}}(t) = d \sin(2\pi f_{\text{vib}} t) \quad (17.41)$$

where f_{vib} is the vibration frequency.

Let the normalized complex echo corresponding to a stationary pixel be $e^{j2\pi f_d t}$, where f_d is the doppler frequency characteristic of the pixel. (We assume low fractional bandwidth, in which case this is equivalent to the doppler frequency corresponding to the center frequency of the transmitted bandwidth; see Section 8.1.5 of Sullivan¹).

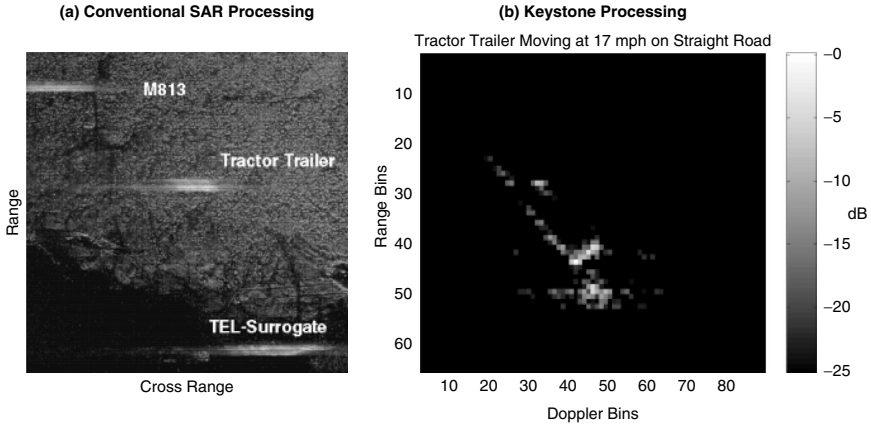


FIGURE 17.11 Imaging a moving target in a SAR image: (a) Conventional SAR image (real data) showing blurred moving vehicles: an M813 military truck, a tractor-trailer truck, and a surrogate (mockup) of a missile transporter-erector-launcher. (b) Image of tractor-trailer truck using “keystone” processing; the truck’s cab is at the bottom and the trailer is above it. (after R. P. Perry *et al.*⁵⁰ © IEEE 1999)

In addition to this echo, the pixel containing the target will produce an additional echo with a periodic *phase error*:

$$\phi_e = \frac{4\pi d}{\lambda} \sin(2\pi f_{\text{vib}} t) = \phi_o \sin(2\pi f_{\text{vib}} t) \quad (17.42)$$

We assume $4\pi d \ll \lambda$, thus $\phi_o \ll 1$. The normalized complex echo corresponding to the phase error is

$$e^{j\phi_e} = e^{j\phi_o \sin(2\pi f_{\text{vib}} t)} \quad (17.43)$$

$$\approx 1 + j\phi_o \sin(2\pi f_{\text{vib}} t) \quad (17.44)$$

$$= 1 + \frac{\phi_o}{2} (e^{j2\pi f_{\text{vib}} t} - e^{-j2\pi f_{\text{vib}} t}) \quad (17.45)$$

The normalized complex echo corresponding to the vibrating target is then the complex product of the echo corresponding to the stationary pixel and the echo corresponding to the phase error:

$$e^{j\phi_{\text{dop}}} = e^{j2\pi f_d t} e^{j\phi_e} \quad (17.46)$$

and

$$e^{j\phi_{\text{dop}}} = e^{j2\pi f_d t} + \frac{\phi_o}{2} (e^{j2\pi t(f_d + f_{\text{vib}})} - e^{j2\pi t(f_d - f_{\text{vib}})}) \quad (17.47)$$

In the SAR image, the vibrating point target will appear in three crossrange locations. Most of the target energy still appears at the correct location, whereas a small fraction of the energy will appear in each of two pixels separated in crossrange by f_{vib} in doppler frequency. Thus, a vibrating target can give rise to a pair of distinctive echoes.

The corresponding velocity separation is $\Delta v = \pm f_{\text{vib}} \lambda/2$, and the crossrange displacement is then

$$\Delta r = \frac{\Delta v}{\Omega} = \frac{\Delta v}{V} R = \pm \frac{f_{\text{vib}} \lambda_{\text{avg}} R}{2V} \quad (17.48)$$

where λ_{avg} = average wavelength (assuming low fractional bandwidth). The relative amplitude of each of the paired echoes is

$$\text{Voltage: } \frac{\phi_o}{2} = \frac{2\pi d}{\lambda_{\text{avg}}} \quad (17.49)$$

$$\text{Power: } \left(\frac{\phi_o}{2}\right)^2 = \left(\frac{2\pi d}{\lambda_{\text{avg}}}\right)^2 \quad (17.50)$$

Thus, the amplitude of the paired echoes is proportional to the square of the vibration amplitude, and crossrange displacement is proportional to the vibration frequency (see Section 7.5.2 of Sullivan¹).

For bright, point-like targets, or for targets such that $4\pi d$ is not small compared to λ , additional terms should be retained in Eq. 17.44, describing the fact that a series of paired echoes, of decreasing amplitude, may appear in crossrange.

Figure 17.12 shows a SAR image of a scene including a vibrating target—a truck with its engine running. The image contains two sets of paired echoes, corresponding to two vibration frequencies characteristic of the particular truck used for the observation.

Measurement of Object Height. The basic theory of SAR assumes that the scene is flat. To the extent that the scene is not flat, distortions in the SAR image will result. In some cases, they can be used to measure the height of elevated objects above a flat terrain.

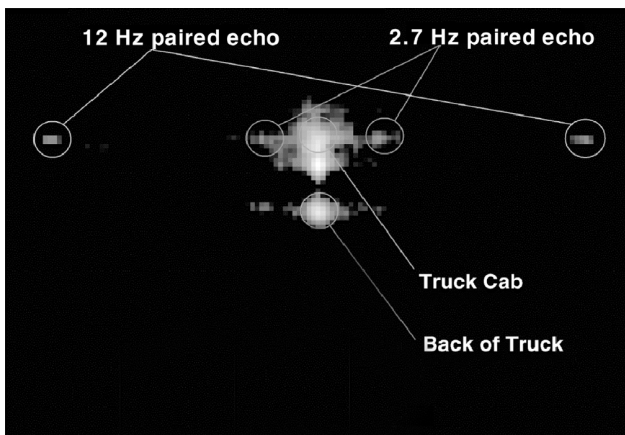


FIGURE 17.12 SAR scene containing vibrating target: Crossrange is horizontal; range is vertical. The paired echoes in crossrange are characteristic of a vibrating target (truck with engine running) in a SAR image. The frequencies (2.7 Hz and 12 Hz) are peculiar to the specific truck that was imaged. (Courtesy of Northrop-Grumman Corporation)

Shadows. The simplest method of measuring object height is to observe the length L_{shadow} of the shadow of the object cast by the SAR and calculate the object height h from the known SAR altitude H and ground range R_g :

$$h = L_{\text{shadow}} \cdot \frac{H}{R_g} \quad (17.51)$$

This expression assumes flat-earth, and may be generalized to curved-earth if R_g is relatively large; see Section 3.2.2 of Sullivan.¹ However, the shadow method works only for an isolated, relatively high object on essentially flat terrain (e.g., Figure 17.9).

Layover. SAR processing sorts target returns into bins (pixels) depending on the range R and velocity v of the target relative to the platform. If two or more targets have the same R and v , then they will be placed at the same location in the SAR image.

We shall define a *layover contour* as the locus of points in 3D space such that an object at any of the points will be assigned to the same location in a SAR image. As shown in Figure 17.13, a layover contour is the intersection of a constant-range sphere of range R and a constant velocity cone of generating angle $\beta = \cos^{-1}(v/V)$ with axis along the platform direction, i.e., a circle of radius $R \sin \beta$ ahead of the platform. ($\beta > 90^\circ$ corresponds to targets behind the platform.) We shall, therefore, call the contour the *layover circle*. If the top of an elevated object, such as a tower, is on the layover circle and if the ground is flat, then the top of the tower will appear in the SAR image at the same position as a point on the ground where the layover circle intersects the ground. The tower will be “laid over,” hence the nomenclature.

As shown in Figure 17.13, let us consider a platform in straight-line, constant-speed motion at altitude H over a flat earth forming a SAR image, the center of which is at slant range $R_s \gg H$ and squint angle θ_{sq} . Suppose that a tower of height h ($h \ll H$) is in the area that is imaged. We describe locations within the image by a coordinate system (x_1, y_1) . If the base of the tower is at (x_{10}, y_{10}) , we wish to ascertain the image coordinates of the top of the tower.

Figure 17.13a illustrates a perspective view. Because $R_g \gg H$, the isodop (y_1 -axis) makes an angle θ_{sq} with the y -axis. The image center is a distance $S \equiv R_g \cos \theta_{\text{sq}}$ from the x -axis, where R_g = ground range. Figure 17.13b shows a view from the $+x$ -axis, indicating the layover circle normal to the x -axis and showing that the image location of the tower top is located a distance (the *layover distance*) $d \equiv hH/(R_g \cos \theta_{\text{sq}})$ from the image location of the tower base. Figure 17.13c then depicts the view in image coordinates (x_1, y_1) . The image coordinates of the tower top are

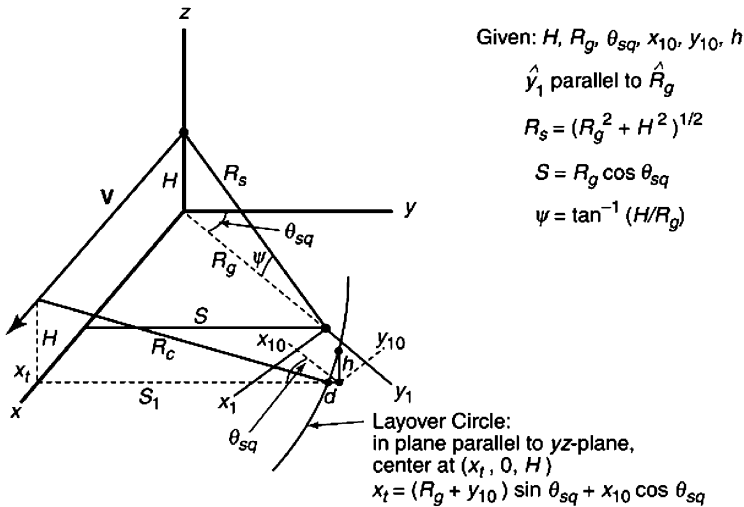
$$x_{11} = x_{10} + d \sin \theta_{\text{sq}}, \quad y_{11} = y_{10} - d \cos \theta_{\text{sq}}$$

For example, if $R_g = 100$ km, $H = 5$ km, $h = 100$ m, and $\theta_{\text{sq}} = 0$, then $d = 5$ m, $x_{11} = x_{10}$, and $y_{11} = y_{10} - 5$ m. The tower top appears in the image 5 m closer to the radar than the tower base. This principle may sometimes be used to estimate the height of isolated, tower-like structures on relatively level ground:

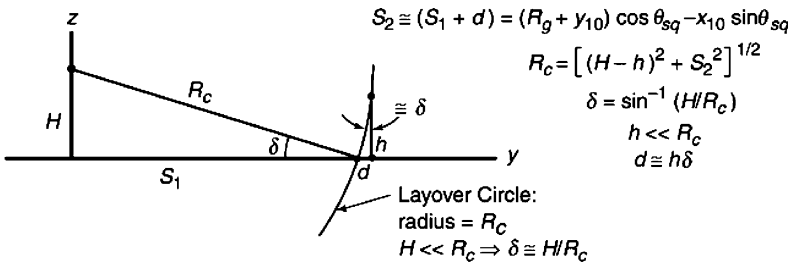
$$h \equiv \frac{dR_g \cos \theta_{\text{sq}}}{H} \quad (17.52)$$

The intersection of the constant-velocity cone and the ground is a hyperbola. If H is not $\ll R$, the isodop direction will not be parallel to the down-range direction.

(a) Perspective View



(b) View from +x axis



(c) View in $x_1 y_1$ (Image) System

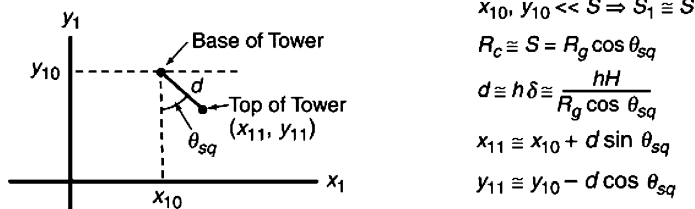


FIGURE 17.13 Layover: (a) Perspective view, (b) view along platform flight path, and (c) view in coordinate system of SAR image (*Courtesy of SciTech Publishing, Inc.*)

The geometry is more complicated but layover distance and object height may still be estimated.

Stereo SAR. Two SAR images of the same scene may be obtained from somewhat different locations (see Section 9.3.8.1 in Carrara et al.³). Noncoherent comparison

of the two—the *stereo* technique—may enable estimation of object height. The technique is analogous to the method by which we humans use our two eyes to help estimate the distance of the objects that we see. In fact, the two SAR images may be printed on the same page using two different colors, with the viewer using special glasses so that the left eye sees only one image and the right eye only the other and the brain processing the two together so that the scene is perceived in 3D.

Interferometric SAR (InSAR) for Target Height Measurement. Interferometric SAR (InSAR)^{42,51,52} (also called IFSAR; see Section 9.3 of Carrara et al.³ and Adams et al.²⁰), when used for terrain height measurement, involves two SAR images taken from antennas at slightly different altitudes and compared *coherently* to obtain fine-resolution information regarding the height of terrain or targets in the image. (In this case, it is sometimes called IFSARE, where *E* emphasizes elevation measurement.) InSAR may be performed using a single platform with two antennas (*single-pass InSAR*) or by the same platform making two passes over the same terrain (*two-pass InSAR*). Allen⁴² gives several examples of fielded systems using each type. It is essential that the relative locations of the two antennas be rather precisely known. Advantages and disadvantages of the two types of InSAR are as follows.

Two-pass InSAR:

- No special hardware is required; a conventional SAR may be flown twice over the designated terrain.
- Motion compensation is challenging; the position of the antenna versus time in each pass must be known with great precision.
- A long baseline (vertical distance between antenna paths) provides fine vertical resolution (but challenging ambiguities).
- The scene may change between passes due to wind, etc.
- Example results are given by Schuler et al.,⁵³ who perform “terrain topography measurement using multipass polarimetric SAR.”

Single-pass InSAR:

- Baseline is relatively well known, providing consistency throughout synthetic aperture.
- Scene is same for both images since data for each are collected simultaneously.
- On-board, real-time processing is a possibility.
- More sophisticated (expensive) hardware is required: two antennas, two receiver channels, and two sets of analog-to-digital (A/D) converters.
- Example results are given by Adams et al.,²⁰ who include an InSAR image of the stadium at the University of Michigan in Ann Arbor, viewable with two-color glasses.

To understand the theory of InSAR, we first consider two antennas, *A* and *B*, separated vertically by a baseline *L*, observing a point target *a* that is on a flat ground at range *R*; the radar line-of-sight (LOS) intersects the flat ground at grazing angle ψ_1 (Figure 17.14). We consider two possibilities: (1) one antenna transmits and each receives ($n = 1$), and (2) antenna *A* transmits and then receives; then antenna *B* transmits and then receives ($n = 2$).

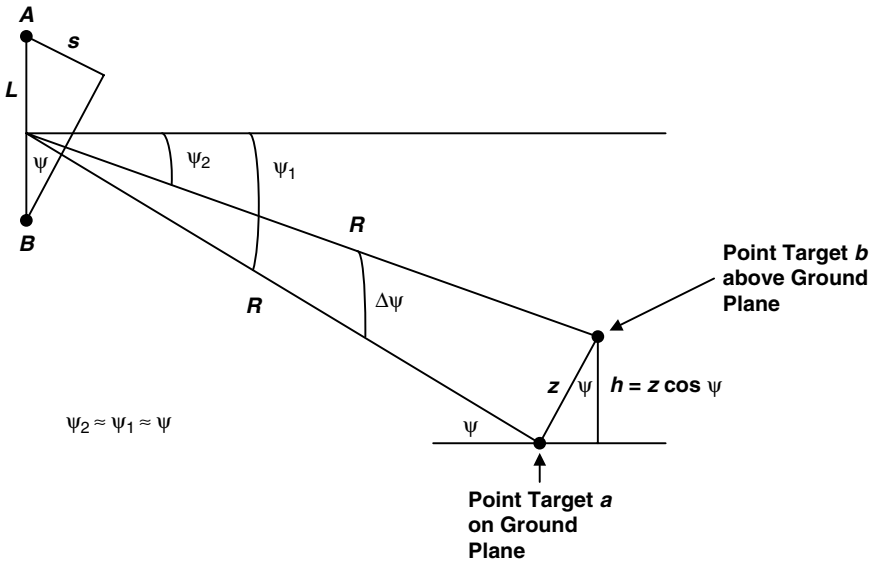


FIGURE 17.14 InSAR—vertical antenna separation: Vertical antenna separation enables estimation of the height of a target above the average ground height or, more generally, terrain height versus location. (*Courtesy of SciTech Publishing, Inc.*)

For a “single-frequency” pulse of wavelength λ , the difference in the phases of the echoes received from the point target observed by the two antennas is (from Figure 17.14)

$$\Delta\phi_1 = \frac{2\pi ns}{\lambda} = \frac{2\pi nL \sin\psi_1}{\lambda} \quad (17.53)$$

We now consider the same antennas A and B observing a second point target b that is a distance h above the flat ground also at range R ; the radar line-of-sight (LOS) intersects the parallel to the flat ground at grazing angle ψ_2 . The difference in the phases of the echoes received from the point target observed by the two antennas is now

$$\Delta\phi_2 = \frac{2\pi nL \sin \psi_2}{\lambda} \quad (17.54)$$

We consider the quantity

$$\Delta\phi \equiv |\Delta\phi_2 - \Delta\phi_1| = \frac{2\pi nL}{\lambda} |\sin\psi_2 - \sin\psi_1| \quad (17.55)$$

We assume that $h \ll R$ and thus $\psi_2 \approx \psi_1 \approx (\psi_2 + \psi_1)/2 = \psi$. Then, where $\Delta\psi = |\psi_2 - \psi_1|$, from Figure 17.14,

$$\Delta\phi \approx \frac{2\pi nL}{\lambda} \cos\psi \Delta\psi = \frac{2\pi nL}{\lambda} \cos\psi \frac{h}{R \cos\psi} = \frac{2\pi nLh}{\lambda R} \quad (17.56)$$

We now consider $|\delta(\Delta\phi)|$ = the change in $\Delta\phi$ due to a change in h given by $|\delta h|$:

$$|\delta(\Delta\phi)| = \frac{2\pi nL}{\lambda R} |\delta h| \quad (17.57)$$

Antennas A and B may be considered as separated in vertical distance on an aircraft. The relationship between $\delta(\Delta\phi)$ and a variation in terrain altitude δh is

$$|\delta h| = \frac{\lambda R |\delta(\Delta\phi)|}{2\pi nL} \quad (\text{antennas separated vertically}) \quad (17.58)$$

InSAR for terrain elevation measurement can also be performed by an aircraft with two antennas separated *horizontally* (perpendicular to the flight path) by L . The aircraft is banking at angle $\gamma > 0$ and collecting data from the flat ground at grazing angle ψ (Figure 17.15). Then the effective aperture (perpendicular to the LOS) is $L \sin(\psi + \gamma)$ instead of $L \cos \psi$. From Figure 17.15, we have

$$|\delta h| = \frac{\lambda R |\delta(\Delta\phi)| \cos \psi}{2\pi nL \sin(\psi + \gamma)} \quad (\text{antennas separated horizontally}) \quad (17.59)$$

In either geometry, since both channels are noisy, the expected accuracy in the phase difference (1-sigma) is given by Levanon¹⁷:

$$\delta(\Delta\phi) = \frac{1}{\sqrt{\text{SNR}}} \sqrt{2} \quad (17.60)$$

where SNR = signal-to-noise ratio (see Section 17.6). Thus, the theoretical accuracy for terrain altitude measurement is

Vertical antenna separation (no banking):

$$\delta h = \frac{\lambda R}{\pi nL \sqrt{2\text{SNR}}} \quad (17.61)$$

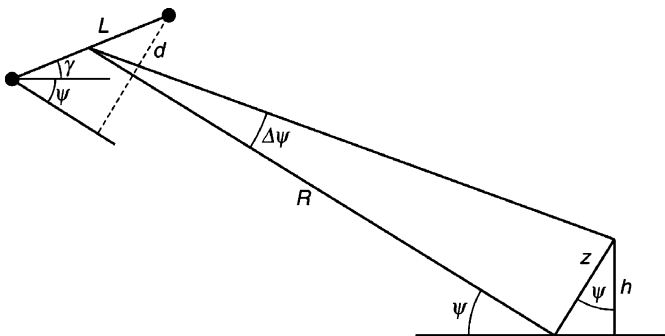


FIGURE 17.15 InSAR—horizontal antenna separation: As long as the two apertures do not both lie on the same line of sight to the target area, an estimate of terrain height may be made, by comparing the phases of echoes received by the two apertures. (Courtesy of SciTech Publishing, Inc.)

Horizontal antenna separation:

$$\delta h = \frac{\lambda R \cos \psi}{\pi n L \sin(\psi + \gamma) \sqrt{2 \text{SNR}}} \quad (17.62)$$

Furthermore, when the phase moves through an interval of 2π , an ambiguity occurs in terrain altitude measurement. The corresponding altitude difference is computed by replacing $\delta(\Delta\phi)$ by 2π in Eqs. 17.58 and 17.59.

Vertical antenna separation (no banking):

$$\Delta h(\text{ambig}) = \frac{\lambda R}{nL} \quad (17.63)$$

Horizontal antenna separation:

$$\Delta h(\text{ambig}) = \frac{\lambda R \cos \psi}{nL \sin(\psi + \gamma)} \quad (17.64)$$

Although we have derived these relationships for a single monochromatic pulse, they can be shown (see Section 8.1.5 of Sullivan¹ and Sections 3.0 and 9.3 of Carrara et al.³) to be true for SAR pixels also, with λ replaced by clf_{avg} .

The National Aeronautics and Space Administration (NASA) performed successful X/C-band single-pass polarimetric InSAR (single-pass) for the Space Shuttle Radar Topography Mission (SRTM), using antennas on the shuttle itself and on the shuttle's maneuverable arm to produce a complete 3D map of the Earth's surface between 60° N latitude and 56° S latitude—nearly 80% of the surface, with best vertical accuracy of 6 meters on a 30-meter horizontal grid.⁵⁴

Foliage-Penetration (FOPEN) SAR. Although higher frequency (greater than approximately 2 GHz) microwaves do not penetrate foliage well, lower frequency microwaves do (Fleishman et al.⁵⁵; see also Section 21-6 of Ulaby et al.⁵⁶). For example, for C band, the attenuation of a typical forest canopy varies from ≈ 10 dB to ≈ 40 dB; the probability that the attenuation is less than 20 dB is about 0.2. On the other hand, for UHF radiation, attenuation varies from 0 to ≈ 20 dB; half the time it is less than ≈ 7 dB. Thus, for FOPEN, UHF radiation is necessary: shorter waves will not penetrate the foliage, whereas for airborne applications, longer waves would require prohibitively large antennas. (Specific values of attenuation [dB/meter] vary with grazing angle, tree type, leaf density, and moisture content; however, the previous statement is a general summary of these results; further details are given in Fleishman et al.⁵⁵)

The aperture time t_A required to collect sufficient data for a SAR image is found from Eq. 17.6. For example, let us assume $R = 100$ km, $V = 180$ m/sec (350 kts), $\theta_{\text{sq}} = 0$, and $\delta_{\text{cr}} = 1$ m. For $f = 10$ GHz (X band, $\lambda = 0.03$ m), $t_A = 8.3$ sec, and the fractional bandwidth $B/f_o = 0.015$. On the other hand, for $f_o = 0.5$ GHz (UHF, $\lambda = 0.6$ m), $t_A = 167$ sec = 2.8 min and $B/f_o = 0.3$. Such a high fractional bandwidth (an *ultra-wideband SAR*) presents challenges in designing hardware components, such as antennas, that are reasonably linear over the full frequency range.⁵⁷ Furthermore, the long aperture time presents motion-compensation challenges, and the wide real-beam angle adds to processing difficulties, very likely requiring Range-Migration Algorithm (RMA) processing (Section 17.3). In addition, for calculating crossrange resolution, the small-angle approximation no longer holds.

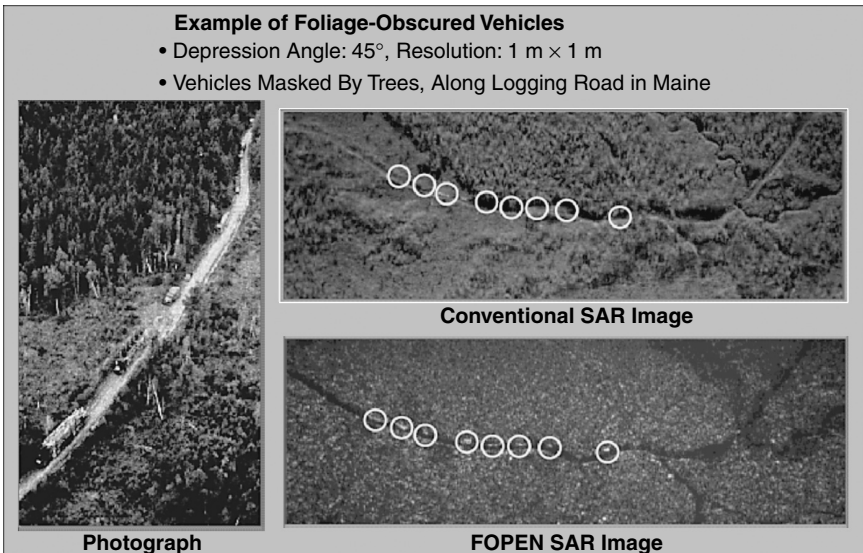


FIGURE 17.16 Conventional and FOPEN SAR⁶² images: In the conventional image, target vehicles cannot readily be seen, whereas in the FOPEN image they are quite prominent. (Source: http://www.darpa.mil/DARPATech2000/Presentations/spo_pdf/4MoyerCCTB&W.pdf)

A number of authors report successful results with FOPEN SAR, using such SARs as the Environmental Research Institute of Michigan P-3 SAR,^{58,59} the Swedish National Defense Research Establishment CARABAS sensor,⁶⁰ and the SRI International Ultra-Wideband SAR.⁶¹ Furthermore, Moyer⁶² presents images from conventional and FOPEN SARs showing that vehicles under trees may be imaged significantly better with FOPEN SAR than with conventional SAR; example imagery is given in Figure 17.16.

REFERENCES

1. R. J. Sullivan, *Radar Foundations for Imaging and Advanced Concepts*, Raleigh, NC: SciTech, 2004; previously published as *Microwave Radar: Imaging and Advanced Concepts*, Norwood, MA: Artech House, 2000.
2. L. J. Cutrona, "Synthetic aperture radar," in M. Skolnik, *Radar Handbook*, 2nd Ed., New York: McGraw-Hill, 1990; 1st Ed., New York: McGraw-Hill, 1970.
3. W. G. Carrara, R. S. Goodman, and R. M. Majewski, *Spotlight Synthetic Aperture Radar*, Norwood, MA: Artech House, 1995.
4. J. Curlander and R. McDonough, *Synthetic Aperture Radar*, New York: John Wiley and Sons, 1991.
5. G. W. Stimson, *Introduction to Airborne Radar*, 2nd Ed., Mendham, NJ: SciTech, 1998.
6. C. J. Jakowatz, Jr., D. E. Wahl, P. H. Eichel, D. C. Ghiglia, and P. A. Thompson, *Spotlight-Mode SAR: A Signal-Processing Approach*, Boston: Kluwer Academic Publishers, 1996.
7. S. A. Hovanessian, *Introduction to Synthetic Array and Imaging Radars*, Norwood, MA: Artech House, 1980.

8. R. O. Harger, *Synthetic Aperture Radar Systems: Theory and Design*, New York: Academic Press, 1970.
9. R. Birk, W. Camus, E. Valenti, and W. McCandless, "Synthetic aperture radar imaging systems," *IEEE AES Magazine*, pp. 15–23, November 1995.
10. C. Jackson and J. Apel (deceased; the book is dedicated to him), *Synthetic Aperture Radar Marine User's Manual*, Washington, DC: Department of Commerce, National Oceanic and Atmospheric Administration (NOAA), 2004.
11. D. Ausherman, A. Kozma, J. Walker, H. Jones, and E. Poggio, "Developments in radar imaging," *IEEE Transactions on Aerospace and Electronic Systems*, vol. AES-20, no. 4, July 1984.
12. C. Wiley, "Synthetic aperture radars," *IEEE Transactions Aerospace and Electronic Systems*, vol. AES-21, pp. 440–443, May 1985.
13. L. J. Cutrona, W. E. Vivian, E. N. Leith, and G. O. Hall, "A high-resolution radar combat-surveillance system," *IRE Transactions on Military Electronics*, vol. MIL-5, no. 2, pp. 127–131, April 1961. (Reprinted in Kovaly.¹⁵)
14. C. W. Sherwin, J. P. Ruina, and R. D. Rawliffe, "Some early developments in synthetic aperture radar systems," *IRE Transactions on Military Electronics*, vol. MIL-6, no. 2, pp. 111–115, April 1962. (Reprinted in Kovaly.¹⁵)
15. J. J. Kovaly, *Synthetic Aperture Radar*, Norwood, MA: Artech House, 1976. (This is a collection of early classic papers concerning SAR.)
16. D. C. Schleher, *MTI and Pulsed Doppler Radar*, Norwood, MA: Artech House, 1991.
17. N. Levanon, *Radar Principles*, New York: Wiley-Interscience, 1988.
18. R. M. Goldstein and H. A. Zebker, "Interferometric radar measurement of ocean currents," *Nature*, vol. 328, pp. 707–709, 1987.
19. R. M. Goldstein, H. A. Zebker, and T. P. Barnett, "Remote sensing of ocean currents," *Science*, vol. 246, pp. 1282–1285, 1989.
20. G. F. Adams et al., "The ERIM interferometric SAR: IFSAR," in *Proceedings of the 1996 IEEE National Radar Conference*, 1996, pp. 249–254. (Reprinted in *IEEE AES Systems Magazine*, December 1996.)
21. M. Skolnik, *Introduction to Radar Systems*: 1st Ed., New York: McGraw-Hill, 1962; 2nd Ed., New York: McGraw-Hill, 1980; 3rd Ed., New York: McGraw-Hill, 2001.
22. S. Musman, D. Kerr, and C. Bachmann, "Automatic recognition of ISAR ship images," *IEEE Transactions on Aerospace and Electronic Systems*, vol. 32, no. 4, pp. 1392–1404, October 1996.
23. W. L. Wolfe and G. Zissis (eds.), *The Infrared Handbook*, rev. ed., Ann Arbor, MI: Environmental Research Institute of Michigan (now General Dynamics, Ypsilanti, MI), 1989.
24. M. Richards, *Fundamentals of Radar Signal Processing*, New York: McGraw-Hill, 2005.
25. R. Klemm, *Principles of Space-Time Adaptive Processing*, London: IEE, 2002.
26. E. F. Knott, J. F. Shaeffer, and M. T. Tuley, *Radar Cross Section*, 2nd Ed., Raleigh, NC: SciTech, 2004.
27. E. O. Brigham, *The Fast Fourier Transform and Its Applications*, Englewood Cliffs, NJ: Prentice Hall, 1988.
28. E. D. Kaplan, *Understanding GPS, Principles and Applications*, Norwood, MA: Artech House, 1996.
29. R. W. Bayma and P. A. McInnes, "Aperture size and ambiguity constraints for a synthetic aperture radar," in *Proc. 1975 International Radar Conference*, pp. 499–504. (Reprinted in Kovaly.¹⁵)
30. F. M. Henderson and A. J. Lewis (eds.), *Principles and Applications of Imaging Radar*, New York: Wiley, 1998.
31. C. Oliver and S. Quegan, *Understanding Synthetic Aperture Radar Images*, Norwood, MA: Artech House, 1998.
32. F. J. Harris, "On the use of windows for harmonic analysis with the discrete Fourier transform," *Proceedings of the IEEE*, vol. 66, no. 1, pp. 51–83, January 1978.
33. D. Barton, *Radar Systems Analysis and Modeling*, Norwood, MA: Artech House, 2004.

34. R. J. Sullivan, A. D. Nichols, R. F. Rawson, C. W. Haney, F. P. Dareff, and J. J. Schanne, Jr., "Polarimetric X/L/C-band SAR," in *Proceedings of the 1988 IEEE National Radar Conference*, 1988, pp. 9–14.
35. D. N. Held, W. E. Brown, and T. W. Miller, "Preliminary results from the NASA/JPL multifrequency, multipolarization SAR," in *Proceedings of the 1988 IEEE National Radar Conference*, 1988, pp. 7–8. See also P. A. Rosen et al., "UAVSAR: New NASA airborne SAR system for research," *IEEE Aerospace and Electronic Systems Magazine*, vol. 22, no. 11, pp. 21–28, November 2007.
36. L. M. Novak, M. C. Burl, and W. W. Irving, "Optimal polarimetric processing for enhanced target detection," *IEEE Transactions on Aerospace and Electronic Systems*, vol. 29, no. 1, pp. 234–243, January 1993.
37. L. M. Novak, S. D. Halversen, G. J. Owirka, and M. Hiatt, "Effects of polarization and resolution on SAR ATR," *IEEE Transactions on Aerospace and Electronic Systems*, vol. 33, no. 1, pp. 102–115, January 1997.
38. R. K. Raney, "Synthetic aperture imaging radar and moving targets," *IEEE Transactions of Aerospace and Electronic Systems*, vol. AES-7, no. 3, pp. 499–505, 1971.
39. A. Freeman, "Simple MTI using synthetic aperture radar," in *Proceedings of IGARSS 1984 Symposium*, ESA SP-215, 1984.
40. A. Freeman and A. Currie, "Synthetic aperture radar (SAR) images of moving targets," *GEC J. Res.*, vol. 5, no. 2, pp. 106–115, 1987.
41. S. Werness, W. Carrara, L. Joyce, and D. Franczak, "Moving target algorithms for SAR data," *IEEE Transactions on Aerospace and Electronic Systems*, vol. AES-26, no. 1, pp. 57–67, 1990.
42. C. T. Allen, "Interferometric synthetic aperture radar," *IEEE GRS Society Newsletter*, pp. 6–13, November 1995.
43. S. Barbarossa and A. Farina, "Space-time-frequency processing of synthetic aperture radar signals," *IEEE Transactions on Aerospace and Electronic Systems*, vol. 30, no. 2, pp. 341–358, April 1994.
44. F. M. Staudaher, "Airborne MTI," Chapter 16 in *Radar Handbook*, M. Skolnik (ed.), 2nd Ed., New York: McGraw-Hill, 1990.
45. J. Ward, *Space-Time Adaptive Processing for Airborne Radar*, Technical Report 1015, Lexington, MA: Lincoln Laboratory, Massachusetts Institute of Technology, 1994.
46. J. Guerci, *Space-Time Adaptive Processing for Radar*, Norwood, MA: Artech House, 2003.
47. V. C. Chen and H. Ling, *Time-Frequency Transforms for Radar Imaging and Signal Analysis*, Norwood, MA: Artech House, 2002.
48. L. Cohen, "Time-frequency distributions—a review," *Proceedings of the IEEE*, vol. 77, no. 7, July 1989.
49. R. Guarino and P. Ibsen, "Integrated GPS/INS/SAR/GMTI radar precision targeting flight test results," in *Proceedings Institute of Navigation GPS-95 Conference*, 1995, pp. 373–379.
50. R. P. Perry, R. C. DiPietro, and R. L. Fante, "SAR imaging of moving targets," *IEEE Transactions on Aerospace and Electronic Systems*, vol. 35, no. 1, pp. 188–200, January 1999.
51. J. Rodriguez and J. M. Martin, "Theory and design of interferometric synthetic aperture radar," *IEE Proceedings*, Part F, vol. 139, pp. 147–159, April 1992.
52. R. Bamler and P. Hartl, "Synthetic aperture radar interferometry," *Inverse Problems*, vol. 14, pp. R1 to R54, August 1998. See also F. Gini and F. Lombardini, "Multibaseline cross-track SAR interferometry: A signal-processing perspective," *IEEE Aerospace and Electronic Systems Magazine*, vol. 20, no. 8, Part 2: Tutorials, pp. 71–93, August 2005; M. A. Richards, "A beginner's guide to interferometric SAR concepts and signal processing," *IEEE Aerospace and Electronic Systems Magazine*, vol. 22, no. 9, Part 2: Tutorials, pp. 5–29, September 2007.
53. D. L. Schuler, J-S Lee, T. L. Ainsworth, and M. R. Grunes, "Terrain topography measurement using multipass synthetic aperture radar data," *Radio Science*, vol. 35, no. 3, May–June 2000, pp. 813–832.
54. W. B. Scott, "Flight to radar-map Earth from space," *Aviation Week and Space Technology*, pp. 50–53, September 20, 1999 (Cover Story).

55. J. G. Fleischman, S. Ayasli, E. M. Adams, D. R. Gosselin, M. F. Toups, and M. A. Worris, "Foliage penetration experiment," (series of three papers), *IEEE Transactions on Aerospace and Electronic Systems*, vol. 32, no. 1, pp. 134–166, January 1996. (This series of papers was awarded the 1996 M. Barry Carlton Award; see *IEEE Transactions on Aerospace and Electronic Systems*, vol. 35, no. 4, p. 1472, October 1999.)
56. F. T. Ulaby, R. K. Moore, and A. K. Fung, *Microwave Remote Sensing*, 3 Volumes, Norwood, MA: Artech House, 1986.
57. E. L. Ayers, J. M. Ralston, R. P. Mahoney, P. G. Tomlinson, and J. McCorkle, "Antenna measures of merit for ultra-wide synthetic aperture radar," in *Proceedings of the 1998 IEEE Radar Conference*, 1998, pp. 331–336.
58. N. Vandenberg, D. R. Sheen, S. Shackman, and D. Wiseman, "P-3 ultrawideband SAR: System applications to foliage penetration," *Proceedings SPIE*, vol. 2757, pp. 130–135, 1996.
59. M. F. Toups, L. Bessette, and B. T. Binder, "Foliage penetration data collections and investigations utilizing the P-3 UWB SAR", *Proceedings SPIE*, vol. 2757, p. 136–144, 1999.
60. L. M. H. Ulander and P. O. Frolind, "Precision processing of CARABAS HF/VHF-band SAR data," *Proceedings IEEE Geoscience Remote Sensing Symposium IGARSS 1999*, Hamburg, Germany, vol. 1, 1999, p. 47–49. Also see L.M. Ulander et al., "Detection of concealed ground targets in CARABAS SAR images using change detection," *Proceedings SPIE*, vol. 3721, p. 243–252, *Algorithms for Synthetic Aperture Radar Imagery VI*, E. G. Zelnio (ed.), 1999.
61. E. M. Winter, M. J. Schlangen, and C. R. Hendrikson, "Comparisons of target detection in clutter using data from the 1993 FOPEN experiments," *Proceedings SPIE*, vol. 2230, p. 244–254, *Algorithms for Synthetic Aperture Radar Imagery*, D. A. Giglio (ed.), 1994.
62. L. Moyer, "Counter concealed target technologies," presented at DARPA Tech 2000, http://www.darpa.mil/DARPATech2000/Presentations/spo_pdf/4MoyerCCTB&W.pdf.

